

1 **Experimental multiblast craters and ejecta —**
2 **seismo-acoustics, jet characteristics, craters, and ejecta**
3 **deposits and implications for volcanic explosions**

4 **Ingo Sonder¹, Alison Graettinger², Tracianne B. Neilsen³, Robin S. Matoza⁴,**
5 **Jacopo Taddeucci⁵, Julie Oppenheimer⁶, Einat Lev⁶, Kae Tsunematsu⁷,**
6 **Greg Waite⁸, Greg A. Valentine¹**

7 ¹Center for Geohazards Studies, University at Buffalo, Buffalo, NY, USA

8 ² Department of Earth & Environmental Sciences, University of Missouri Kansas City, Kansas City, MO,
9 USA

10 ³Department of Physics and Astronomy, Brigham Young University, Provo, UT, USA

11 ⁴Department of Earth Science and Earth Research Institute, University of California, Santa Barbara, CA,
12 USA

13 ⁵Istituto Nazionale di Geofisica e Vulcanologia, Rome, Italy

14 ⁶Lamont Doherty Earth Observatory, Columbia University, Palisades, NY, USA

15 ⁷Yamagata University, Yamagata, Japan

16 ⁸Geological and Mining Engineering and Sciences, Michigan Tech, Houghton, MI, USA

17 **Key Points:**

- 18 • Airborne energy of an underground blast decays exponentially with scaled depth
19 and is in agreement with previous measurements.
- 20 • Multiple subsurface explosions, properly timed, can break the surface from scaled
21 depths previously thought to be contained in the ground.
- 22 • Crater sizes correlate with measured seismo-acoustic and high-frequency atmo-
23 spheric signals.

Corresponding author: Ingo Sonder, ingomark@buffalo.edu

24 Abstract

25 Blasting experiments were performed that investigate multiple explosions that occur in
26 quick succession in the ground and their effects on host material and atmosphere. Such
27 processes are known to occur during volcanic eruptions at various depths, lateral loca-
28 tions, and energies. The experiments follow a multi-instrument approach in order to ob-
29 serve phenomena in the atmosphere and in the ground, and measure the respective en-
30 ergy partitioning. The experiments show significant coupling of atmospheric (acoustic)-
31 and ground (seismic) signal over a large range of (scaled) distances (30–330 m, 1–10 m J^{-1/3}).
32 The distribution of ejected material strongly depends on the sequence of how the explo-
33 sions occur. The overall crater sizes are in the expected range of a maximum size for many
34 explosions and a minimum for one explosion at a given lateral location. The experiments
35 also show that peak atmospheric over-pressure decays exponentially with scaled depth
36 at a rate of $\bar{d}_0 = 6.47 \times 10^{-4} \text{ m J}^{-1/3}$; at a scaled explosion depth of $4 \times 10^3 \text{ m J}^{-1/3}$
37 ca. 1% of the blast energy is responsible for the formation of the atmospheric pressure
38 pulse; at a more shallow scaled depth of $2.75 \times 10^{-3} \text{ m J}^{-1/3}$ this ratio lies at ca. 5.5–
39 7.5%. A first order consideration of seismic energy estimates the sum of radiated airborne
40 and seismic energy to be up to 20% of blast energy.

41 Plain Language Summary

42 Blasting experiments using six successive explosions were performed in four differ-
43 ent geometrical setups (linear and triangular). The experiments were monitored by geo-
44 physical equipment which allows to measure explosive energy, and how much of that en-
45 ergy goes to the surface. The experiments help to understand volcanic and other sub-
46 surface explosive processes. Exact measurements of the resulting craters, together with
47 known explosive energies allow the interpretation of real volcanic craters. The experi-
48 mental results show initial time developments of crater sizes, which occurs on the order
49 of one second for crater sizes of the order of one meter. Up to 8% of the explosion’s en-
50 ergy was detected as airborne signal. Up to 20% of the explosion’s energy was detected
51 as seismic (elastic) energy in the ground.

1 Introduction

Volcanic activity causes subsurface explosions at various depths that can have severe consequences for its environment. Explosions can have several causes, but it is possible to evaluate some of their aspects independent from their cause. A sudden, large pressure change propagates at supersonic speed for a certain distance in a medium such as host rock, magma or atmosphere, causing deformation in elastic, plastic and brittle regimes (e.g. Schnurr et al., 2020; Kim & Rodgers, 2016; Bowman et al., 2014; Fee et al., 2013; Taylor et al., 2010; Grady, 1996). Shallow explosions fragment and eject magma, host material or both into the atmosphere and pose danger to the surroundings. Deeper explosions (for a given energy release) may be fully contained in the subsurface (Valentine et al., 2014). In case of a subsurface explosion parts of the energy involved will end up in the atmosphere, while some of it will remain in the ground. In volcanic settings explosions may occur as individual events or in rapid succession, at various depths and lateral locations. Characterizing the transition from a fully contained process to near surface is important to estimate the hazards to surroundings and understand some principle mechanisms of the explosion process. Many mechanisms can cause volcanic explosions (Houghton, 2015), but some effects on the surroundings are common to all explosive source mechanisms. For example, all explosive processes mix host material, and shallow explosions eject significant amounts of hot material (Graettinger et al., 2015). Subsurface explosions produce crater structures, that are characteristic for the blast process's energy and location (Valentine et al., 2014).

In natural settings, explosive volcanic blasts and processes are often monitored using multiple techniques, including seismic and infrasound observation and video recordings at normal and high speeds (Gaudin et al., 2016; Matoza et al., 2019). Seismoacoustics aims to relate signatures of observed seismic and infrasound waveforms to the source processes generating them. A more controlled process than the poorly constrained natural signals, with known source parameters can help to constrain uncertainties and enable scalability of models.

An explosion—a sudden, rapid change of a material's volume that it imposes on its surroundings—forces that medium to rapidly compress such that the resulting pressure change does not propagate with the same speed as a smaller pressure change would which is described within the linear acoustic approximation. Larger pressure changes cause

84 adiabatic heating in air which locally increases the propagation speed and can lead to
 85 dramatic steepening of an initially smooth pressure wave into a discontinuity—a shock
 86 (Garcés et al., 2013; Muhlestein et al., 2012; Crighton & Scott, 1979). In an isentropic
 87 approximation (reversible process at constant entropy) a shock pulse has characteristic
 88 properties such as amplitude and duration that scale with the explosion’s energy and the
 89 density of the medium in which the pulse travels (Kinney & Graham, 1985).

90 Scaling properties enable the establishment of phenomenological regimes that de-
 91 pend on scaled parameters, such as a scaled length. For example, for the depth d of a
 92 subsurface explosion, a scaled depth can be defined by

$$\bar{d} = \frac{d}{E_b^{1/3}} \quad , \quad (1)$$

93 where E_b is the blast’s energy (Holsapple & Schmidt, 1980; Sonder et al., 2015). Using
 94 this method blasts of any energy may be categorized into deep, intermediate and shal-
 95 low blasts. Deep blasts are contained in the ground and do not eject material ($\bar{d} \gtrsim 8 \times 10^{-3} \text{ m J}^{-1/3}$).
 96 The host material’s weight and strength are large enough to “contain” the blasts. En-
 97 ergy is dissipated by friction and anelastic alteration, or transported elastically as seis-
 98 mic waves. At intermediate scaled depths ($\bar{d} \simeq 4 \times 10^{-3} \text{ m J}^{-1/3}$), material is excavated
 99 efficiently, which results in the largest craters. Shallow blasts ($\bar{d} < 4 \times 10^{-3} \text{ m J}^{-1/3}$) cre-
 100 ate a smaller crater. Larger parts of E_b couple with the atmosphere and fewer with the
 101 host, resulting in a large atmospheric pressure pulse. These regimes are backed up by
 102 extensive studies from military and mining research (Holsapple & Schmidt, 1980; Lee
 103 & Mazzola, 1989; Ehergott et al., 2011; Dillon, 1972; Qiu et al., 2018), as well as research
 104 motivated by volcanology (Ambrosini et al., 2002; Sato & Taniguchi, 1997; Goto et al.,
 105 2001; Valentine et al., 2012; Sonder et al., 2015; Ross et al., 2013). Two lengths which
 106 scale with the 1/3 power of E_b and which differ by a factor 2, for example two crater radii
 107 created by two single subsurface blasts, were caused by blast energies which differed by
 108 a factor $2^3 = 8$.

109 Similar phenomenological regimes exist for a blast wave propagating in air. The
 110 distance from explosion source, r , may be scaled by blast energy and air density ρ

$$\bar{r} = \frac{\rho r}{\rho_0 E_b^{1/3}} \quad . \quad (2)$$

111 The reference density ρ_0 is a value known from a case for which the scaled distance is
 112 known. Similar to \bar{d} , \bar{r} may be used to categorize an observation distance into far ($\bar{r} \gtrsim$

113 $6 \times 10^{-2} \text{ m J}^{-1/3}$), in which the peak pressure drops with \bar{r}^{-1} , intermediate ($\bar{r} \simeq 6 \times 10^{-3} \text{ m J}^{-1/3}$),
 114 or near ($\bar{r} \lesssim 10^{-3} \text{ m J}^{-1/3}$), (Kinney and Graham (1985)).

115 Less studied, from a volcanological perspective, is the effects of scaled depth on mon-
 116 itoring signals such as seismic, acoustic, and infrasound, particularly in cases involving
 117 multiple explosions occurring in rapid succession. Crater structures and ejecta products
 118 of such blasts are analyzed, and allow to connect their geometries and stratigraphy to
 119 energy, explosion locations and sequencing. These field findings also reveal the complex-
 120 ities of the natural processes, which limit the straight forward application of simple ex-
 121 plosion models (Taddeucci et al., 2010). Some factors controlling the dynamic behav-
 122 ior and energy scaling have a common base with other applications of explosives in the
 123 fields of military or mining research (Ambrosini & Luccioni, 2006; Qiu et al., 2018). Such
 124 applications allow the scaling of lengths with a blast’s energy, and use the depth below
 125 the surface to quantify its confinement. The scaling relationships were found experimen-
 126 tally, and while in detail the phenomena associated with a subsurface explosion depends
 127 on factors such as host material strength, rough phenomenological regimes can be iden-
 128 tified that are primarily related to energy and depth combinations. Energy scaling was
 129 experimentally verified across length scales ranging from 10^{-2} m to 10^3 m , and energies
 130 from 10^3 J to 10^{15} J (Strange et al., 1960; Vortman, 1968; Sato & Taniguchi, 1997). En-
 131 ergies of most volcanic eruptions fall into this range (Valentine et al., 2014), motivating
 132 either direct applicability of the methods or a version adapted to volcanic activity.

133 Here we report results of experiments that focus on the effects of multiple explo-
 134 sions, closely spaced and timed, on ejecta, crater morphology, and geophysical signals.
 135 Such explosions show different behavior depending on the state of topography and host
 136 conditions at time of explosion. Both are varying rapidly, which causes ejecta jets to be-
 137 come asymmetric (Figure 1, supporting video S1–S4), and can be observed on volcanic
 138 scale (Voight, 1981). A volcanic explosive source was replaced by time- and energy-constrained
 139 chemical explosions. Previous experimental studies showed that this approach has im-
 140 portant implications for field-scale analysis and interpretation (Sato & Taniguchi, 1997;
 141 Goto et al., 2001; Graettinger et al., 2014; Bowman et al., 2014; Valentine et al., 2014,
 142 2015; Sonder et al., 2015; Graettinger et al., 2015; Macorps et al., 2016; Graettinger, Valen-
 143 tine, & Sonder, 2015). In these previous experiments explosive charges were detonated
 144 separately, and the effects of each single detonation on the surface morphology and ejected
 145 material were studied before detonating the next charge. While the approach is relevant



152

153

154

155

157

Figure 1: Side- and top view of a typical asymmetric ejecta jet created by the detonation sequences. Red markers show surface of charge locations. The example shows the jet of the third detonation in the “pad 1” configuration (See also supporting video S1).

146

147

148

149

150

151

to many volcanic settings, observation shows that during explosive eruptions many explosions can occur closely spaced in time (Matoza et al., 2014; Park et al., 2021) or simultaneously, superposing their tephra jets, to create one single cumulative eruption column (Dürig, Gudmundsson, & Dellino, 2015). Our study tests whether the results of previous experiments with separate blasts can be extended to those with blasts in rapid succession and with lateral and vertical migration.

158

2 Methods and Experimental Setup

159

160

161

162

163

164

165

166

167

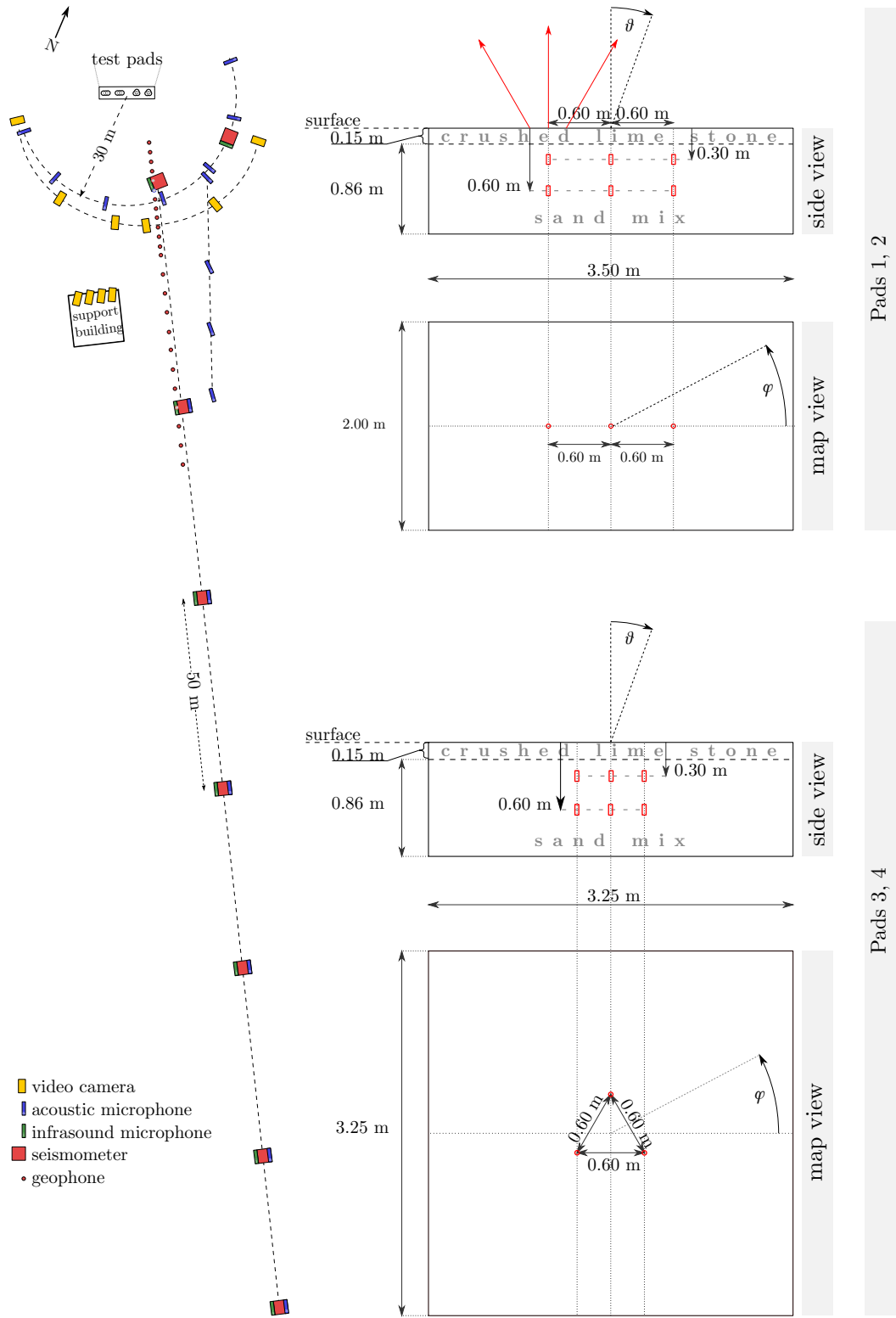
For each of the experiments reported here six charges were buried and detonated in test pads which were filled with unconsolidated granular material. The setup roughly follows previous studies on craters, each of which was created by more than one explosion (“multiblast craters”) in which charges were detonated, and their blasts studied one at a time (Valentine et al., 2012; Graettinger et al., 2014; Sonder et al., 2015). The explosive material was Pentex™, which is a proprietary compound material with major components including trinitrotoluene (TNT) and pentaerythritol (PETN). It has a specific energy of $4.85 \times 10^6 \text{ J kg}^{-1}$; each charge had a mass of 90 g which corresponds to an energy of $4.37 \times 10^5 \text{ J}$. The six charges were detonated in a timed sequence of 0.5 s between

168 each detonation. Accuracy of detonation timing was better than 10^{-3} s. This timing was
169 selected to ensure that the ejecta jet of each blast interacted with that of the preceding
170 blast. Two plan-view configurations were set up; one with three charge epicenters in a
171 line; another with three epicenters corresponding to the apexes of a triangle. Charges
172 were arranged vertically on top of one another, at two depths, 30 cm and 60 cm (Figure 2).
173 At the given blast energy 30 cm corresponds to a scaled explosion depth of $3.95 \times 10^{-3} \text{ m J}^{-1/3}$,
174 a value very close to optimum excavation conditions. Horizontal spacing was chosen, such
175 that the horizontal neighbor charge location would be within the footprint of a single
176 blast at optimum depth, but close to its border. At pads 1 and 3 the upper charges were
177 detonated in sequence, followed by the three lower charges. At pads 2 and 4, charges be-
178 neath each epicenter were detonated in a sequence of shallow-first and deeper-second (Fig-
179 ure 3).

204 The blast sequences were monitored by high-speed and normal speed video cam-
205 eras. A set of six cameras was arranged in a hemicycle, at a distance between 20–30 m
206 to accurately capture directions of ejected materials. Drone-based video was recorded
207 to determine lateral jet directions and material motion. High-speed cameras recorded
208 at 300, 500 and 5000 fps.

209 Seismo-acoustic records were made using a combination of seismometers, geophones,
210 infrasound-microphones (“infrasound sensors”) and higher frequency broadband micro-
211 phones (“acoustic microphones”). The deployed seismometers and infrasound sensors fit
212 into the SEED broadband category (band code “C”, Ahern & Dost, 2012). Seismome-
213 ters and infrasound sensors were recorded at 400 Hz or 500 Hz. Deployed infrasound sen-
214 sors had a flat frequency response between 3×10^{-2} Hz and Nyquist frequency. Two types
215 of the acoustic microphones were used, with linear (± 2 dB) response from 3.15 Hz to 20 kHz
216 and 4 Hz to 80 kHz (Table 1). Despite the short hand “acoustic microphones” these sen-
217 sors range far into the ultrasonic range. Recordings in this frequency range are very rare
218 for volcano seismo-acoustics or not available at all. High-frequency recordings typically
219 end around 10 kHz (Taddeucci et al., 2021).

220 From these sensors seismo-acoustic measurement stations were assembled for spe-
221 cific purposes. Station type (a) was dedicated to measure the radial decay of airborne-
222 and ground based blast signals. For each of the type (a) statios a 3-component seismome-
223 ter, an infrasound microphone and two acoustic microphones were used. The seismome-



180

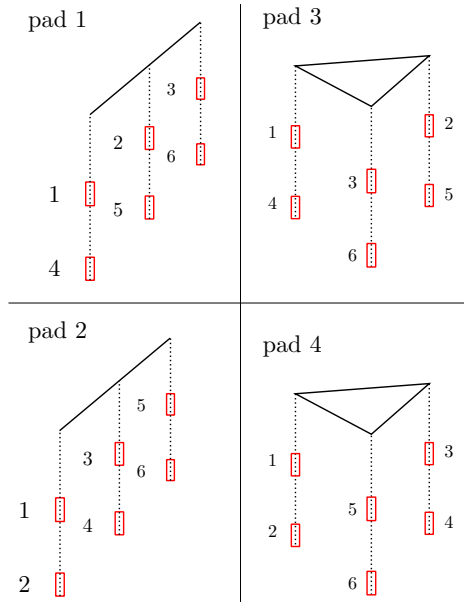
182

Figure 2: (Caption on next page)

183 **Figure 2:** Multi-sensor stations were placed in a radial line every 50 m starting at 30 m
 184 distance from the test pads. Each station included compact broadband seismic and in-
 185 frasonic sensors as well as broadband (“acoustic”) microphones. Acoustic microphones
 186 were placed in a 30 m radius semicircle around the center of the test pads. Another set
 187 of microphones was placed in a radial line from the test pads ranging from 30 m to 80 m
 188 distance. 12 geophones were placed every 2.5 m starting at 12 m distance from the pads
 189 center, and 11 more along the same direction every 5 m following that. The last geophone
 190 had a distance of 99.5 m from the pads center. Six identical cameras recorded the experi-
 191 ments also in an arc of about 30 m distance. Other cameras recorded from a 50 m distance
 192 location.

224 ter was placed 1 m below-, the infrasound sensor just below the surface. The microphones
 225 were mounted 4 m above ground, pointing towards the blast source, and just above ground,
 226 pointing downwards. Seven type (a) stations were placed every 50 m in a radial line, start-
 227 ing at 30 m distance from the test pads center, so that the last station was at 380 m dis-
 228 tance (Figure 2). Station type (b) was dedicated to the depth dependency of blast sig-
 229 nals. One station was assembled which consisted of three 3-component seismometers, placed
 230 132 cm, 75 cm and 18 cm below the surface, and one infrasound sensor, placed just be-
 231 low the surface. Station (b) had a distance of 30 m from the blast pads center (Figure 2).
 232 Station type (c) was dedicated to measure the angular dependency of the airborne sig-
 233 nals. For each of them two acoustic microphones were placed 2.44 m and 1.22 m above
 234 ground. Type (c) stations were placed in a 30 m radius semi-circle around the center of
 235 the blast pads. Angles range from 0° to 180° and were arranged so that the 90° station
 236 was also the start of the type (a) radial line (Figure 2). Seismo-acoustic setup also in-
 237 cluded a line of 23 geophones to record ground speeds at 12 m–100 m distance along the
 238 type (a) radial line.

239 Ejected material was collected in two box arrays, separated at an angle $> 45^\circ$ to
 240 collect material from 2.5–13.5 m from the charge assembly’s center. The sample arrays
 241 were re-positioned for each experiment, so that they were always centered around an ex-
 242 plosion site. One array was typically at an angle $\phi = 90^\circ$. The other array had differ-



195

196 **Figure 3:** Firing sequence of the four test pads. Numbers indicate the position of the
 197 firing sequence. Charges were fired in one after another in 0.5 s intervals. For any number
 198 i between 1 and 6 the corresponding charge was fired $(i - 1) \cdot 0.5$ s after the first charge.
 199 In pads 1 and 3 the upper charges (buried at 30 cm depth) were the first three to be fired,
 200 before the lower level (buried at 60 cm depth) was fired in the same lateral sequence as
 201 the upper ones. In pads 2 and 4 charge pairs located at same horizontal location were
 202 fired consecutively (upper level 0.5 s before lower level).

Table 1: Sensor setup of the three seismo-acoustic station types.

| Station Type Dependency Deployment | Sensors Per Station ¹ | Vertical Setting (Direction) ² | Sampling Rate | Frequency Range (± 2 dB) ³ | Remarks |
|---|-------------------------------------|---|------------------|--|--|
| type (a) <i>radial</i> 7 stations | seismometer | −1 m | 400 Hz | | Nanometrics 120s Trillium Compact Posthole |
| | infrasound | 0 m | | | |
| | microphone 1 | +4 m (towards blast) | 204.8 kHz | 3.15 Hz – 20 kHz | 1/2" pre-polarized GRAS 40AE, 40AO |
| | microphone 2 | +0.1 m (towards gnd.) | | | |
| type (b) <i>depth</i> 1 station | seismometer 1 | −0.18 m | 500 Hz | | Guralp CMG3ESP 60sec |
| | seismometer 2 | −0.75 m | | | |
| | seismometer 3 | −1.32 m | | 0.03 Hz – 250 Hz | Honeywell Differen- tial Pressure Sensor |
| | infrasound | −0.05 m | | | |
| type (c) <i>angular</i> 6 stations | microphone 1 | +2.44 m | 204.8 kHz | 4 Hz – 80 kHz | 1/4" pre-polarized GRASS 40BE |
| | microphone 2 | +1.22 m | | | |

¹: Each seismometer in any of the stations had three components, North ('N' or '1'), East ('E' or '2') and vertical ('Z'). Components were aligned vertically (positive downward, 'Z'), radially (positive pointing away from the direction of the blast source, 'N', '1' → 'R') and to the transverse direction (perpendicular to radial, 'E' or '2' → 'T').

²: Vertical distance relative to local ground surface: positive above, negative below. Direction in parentheses is the direction of the microphone maximum sensitivity.

³: Upper limit refers either to Nyquist frequency or to sensor limit, see text. The ± 1 dB frequency range of the 40 AE, 40 AO is 5 Hz – 10 kHz; frequency range of the 40 BE is 10 Hz – 40 kHz.

243 ent orientations for each pad, because other equipment and arrangements restricted the
244 available space (Figure 5).

245 After the charges had detonated and ejecta jets had dissipated, photographs of the
246 produced compound craters were taken for photogrammetry (structure from motion) anal-
247 ysis. Photographs were taken using (a) the same UAVs that also recorded blast videos,
248 and (b) using a standard SLR camera, operated by a (ground-based) person. A subset
249 of the photographs was the base for digital elevation models (DEMs) that were created
250 using the commercial photogrammetry software Metashape™, generally following pre-
251 vious experiments (Graettinger, Valentine, & Sonder, 2015). The resulting DEMs have
252 a spatial resolution between 1 cm and 1.5 cm for pads 1–3, and 2.5 cm for pad 4. All crater
253 profiles- and sizes presented below are based on these elevation models.

254 **3 Observations and Results**

255 **3.1 Qualitative Observations**

256 For all pads, the initial blast transported the greatest mass of material. From the
 257 main observation direction this charge was located at the top-left end of the linear se-
 258 tups of pads 1 and 2, and at the top-rear corner of the triangular setups of pads 3 and 4.
 259 Size and speed of these initial blasts (jets) were comparable to previously conducted ex-
 260 periments (Valentine et al., 2012). Ejecta jets of the quieter blasts showed similar thin-
 261 ning behavior as was observed in previous experiments for blasts under pre-existing crater-
 262 topography (Ross et al., 2013; Graettinger et al., 2015). Some jets had a main direction
 263 that was not vertical, but had a certain direction towards the main (temporally chang-
 264 ing) crater void showing similarities with previously conducted off-center blast exper-
 265 iments (Valentine et al., 2015). For pads 2 and 4, for which the lower charges were fired
 266 only 0.5 s after the upper charge (at same lateral location), the perceived loudness (not
 267 measured amplitude) of these lower charges was significantly larger compared to the pre-
 268 vious optimum depth blast. In contrast, for pads 1 and 3, for which lower charges were
 269 fired 1.5 s after the upper charge at same lateral location, the blast noise was significantly
 270 muffled (Table 2).

280 **3.2 Jets, Craters and Ejecta**

281 Unlike past experiments in which a crater was analyzed after each individual blast,
 282 the timing of these multiblast experiments only allows for inspection of the final crater
 283 and ejecta. This crater is the cumulative product of six blasts that migrate vertically and
 284 laterally through the host. The blast sequences in pads 1 and 2 created craters elongated
 285 along the axis of the charges. The final craters of the triangular blast sequences (pads
 286 3 and 4) were more round, with some visibility of single-charge crater outlines in the tri-
 287 angle’s corners (Figure 4).

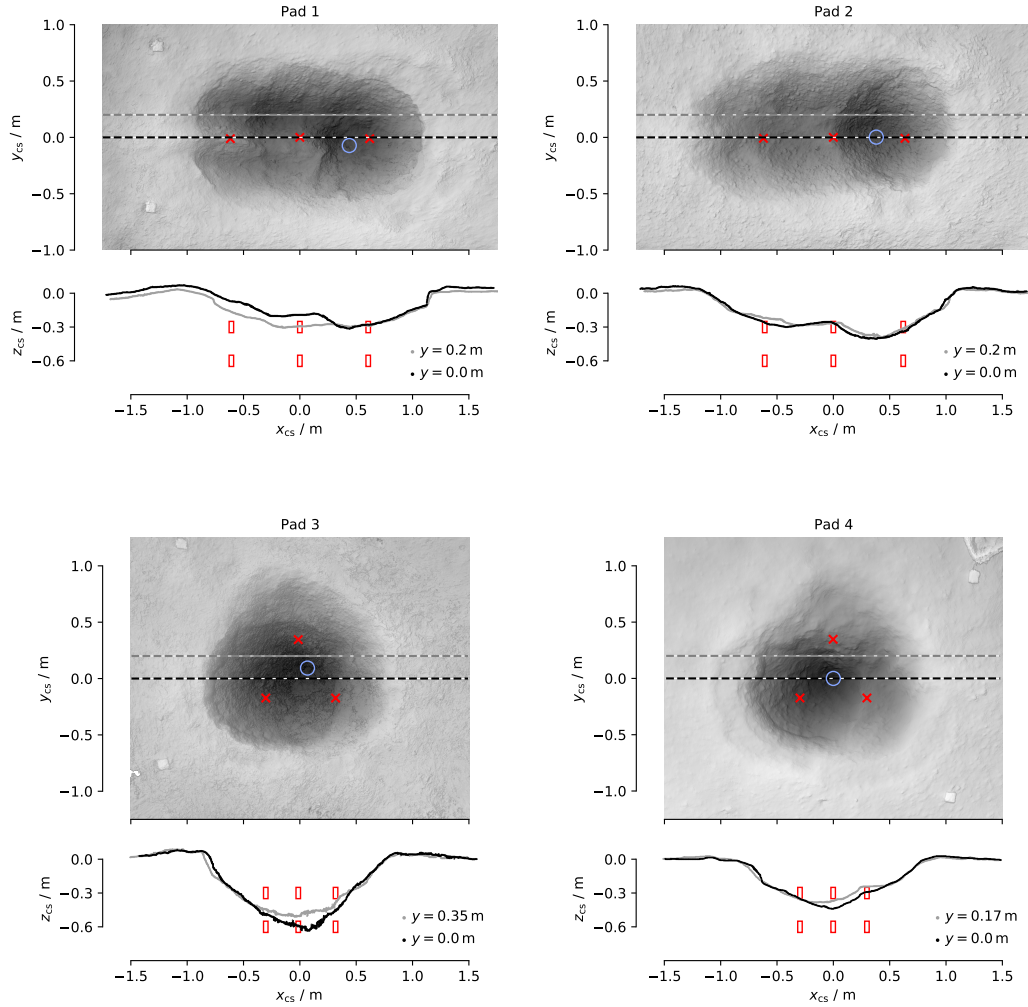
296 The deepest points of the pad 1 and pad 2 craters were located between the cen-
 297 tral and right charge positions in the x -direction, and in close proximity to the symme-
 298 try line along the charges in y -direction. The lower right charge was always the last to
 299 detonate. The crater profiles preserved a stepped floor centered over the final charge (Fig-
 300 ure 4). The ejecta showed a prominent ray (ridge of material) that extended from the
 301 final charge location out of the crater in the direction of elongation ($\varphi = 180^\circ$). Parts

271 **Table 2:** Qualitative comparison of blast experiment configuration and resulting noise
 272 and direction. The “left” and “right” labels refer to the jet directions as seen from the
 273 main observation location. Polar- and inclination angles are also illustrated in Figure 2.

| pad | blast | depth | delay after 1 st chrg. | delay after corresp. chrg. ¹ | perceived loudness | Incli- nation (θ) | approx. polar angle (φ) ² |
|-----|-------|-------|--------------------------------------|--|-----------------------|-------------------------------|---|
| 1 | 1 | 30 cm | 0 s | 0 s | medium | none | – |
| | 2 | 30 cm | 0.5 s | 0 s | medium | > 30° | 180° (left) |
| | 3 | 30 cm | 1 s | 0 s | medium | > 30° | 180° (left) |
| | 4 | 60 cm | 1.5 s | 1.5 s | muffled | none | 0° (–) |
| | 5 | 60 cm | 2 s | 1.5 s | muffled | > 30° | 180° (left) |
| | 6 | 60 cm | 2.5 s | 1.5 s | muffled | > 30° | 180° (left) |
| 2 | 1 | 30 cm | 0 s | 0 s | medium | none | – |
| | 2 | 60 cm | 0.5 s | 0.5 s | loud | none | – |
| | 3 | 30 cm | 1 s | 0 s | medium | > 30° | 180° (left) |
| | 4 | 60 cm | 1.5 s | 0.5 s | loud | > 30° | 180° (left) |
| | 5 | 30 cm | 2 s | 0 s | muffled | > 30° | 180° (left) |
| | 6 | 60 cm | 2.5 s | 0.5 s | loud | \lesssim 20° | 95° (left) |
| 3 | 1 | 30 cm | 0 s | 0 s | medium | none | – |
| | 2 | 30 cm | 0.5 s | 0 s | medium | medium | 135° (left) |
| | 3 | 30 cm | 1 s | 0 s | medium | large | 30° (right) |
| | 4 | 60 cm | 1.5 s | 1.5 s | muffled | low | 270° (–) |
| | 5 | 60 cm | 2 s | 1.5 s | muffled | medium | 150° (left) |
| | 6 | 60 cm | 2.5 s | 1.5 s | muffled | large | 30° (right) |
| 4 | 1 | 30 cm | 0 s | 0 s | medium | none | – |
| | 2 | 60 cm | 0.5 s | 0.5 s | loud | none | – |
| | 3 | 30 cm | 1 s | 0 s | medium | medium | 135° (left) |
| | 4 | 60 cm | 1.5 s | 0.5 s | loud | low | 135° (left) |
| | 5 | 30 cm | 2 s | 0 s | medium | medium | <30° (right) |
| | 6 | 60 cm | 2.5 s | 0.5 s | loud | low | <30° (right) |

275 ¹: Delay of the lower charges, relative to the upper charge at same lateral location (cf.
 276 Figure 3).

277 ²: Polar angle is counted counter clock wise, and 0° along the axis parallel to the charge
 278 lines of pads 1 and 2, pointing to the right as seen from main observation direction.



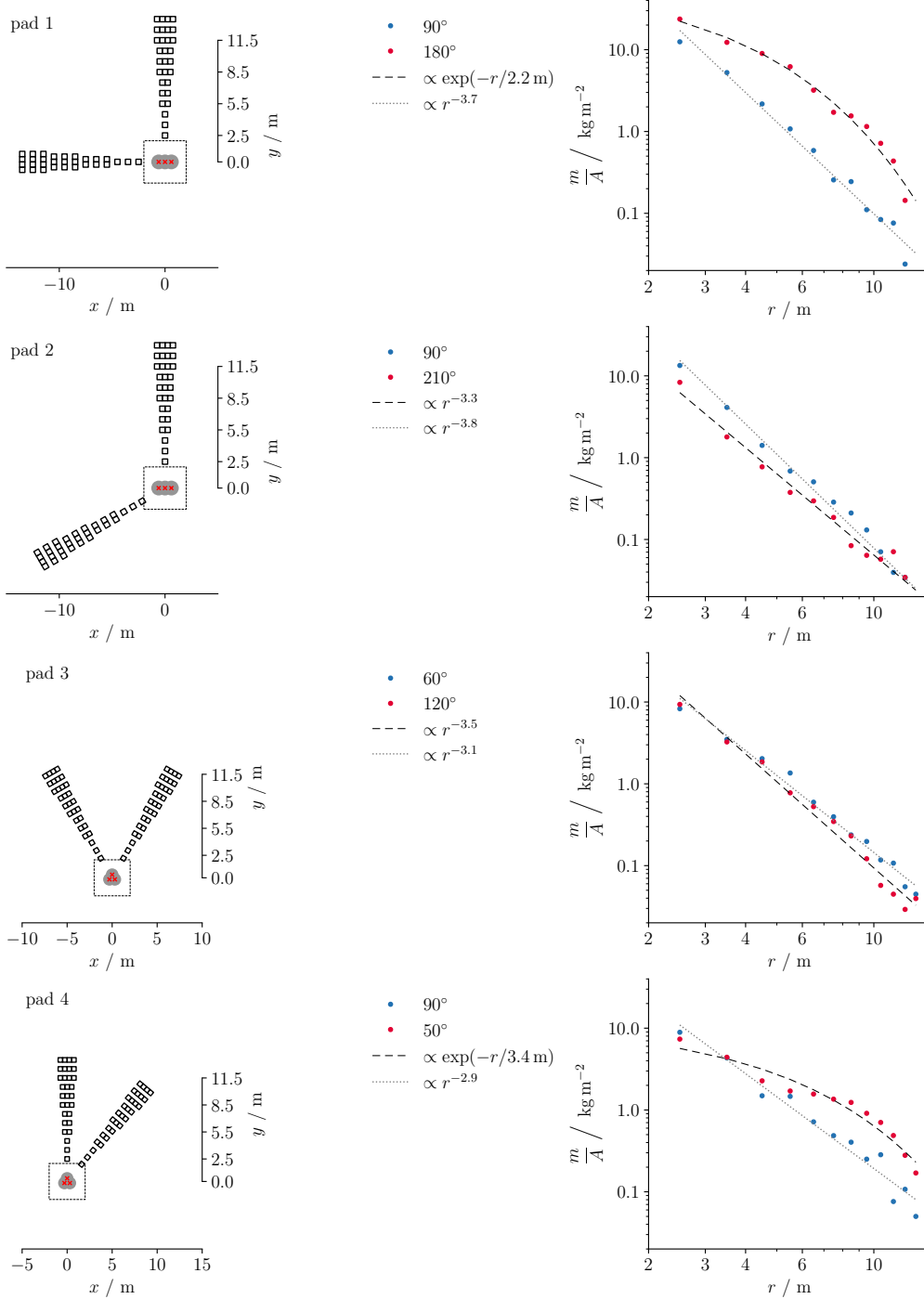
288

289 **Figure 4:** Map view and selected crater profiles of the crater structures. Red crosses
 290 and boxes mark the locations of explosive charges, blue circles show the deepest points of
 291 the craters. The pre-blast surface was at $z_{cs} = 0$. The linear charge arrangements (pads
 292 1 and 2) created a stepped profile that reflect the blast history to some extent. Their
 293 deepest point was about 30 cm, the upper charge depth. Sequences shot in the triangular
 294 geometries (pads 3 and 4) excavated significant amounts of material from below 30 cm.

302 of the ray could be traced more than 10 m from the crater. For pad 1, one of the ejecta
 303 sample arrays was in line with this ray (supplementary video S1); in this direction the
 304 ejected mass per area was a factor $\simeq 10$ higher compared to the material collected by
 305 the array perpendicular to the charge line (Figure 5). Also, mass distribution is better
 306 described by an exponential distribution in the $\varphi = 180^\circ$ -direction compared to the 90° -
 307 direction which is better approximated by a power law. Isolated pieces of shallow-sourced
 308 gravel from pads 1 and 2 were observed further from the charges; one of them over 30 m
 309 away from pad 2, in the $\varphi = 180^\circ$ -direction.

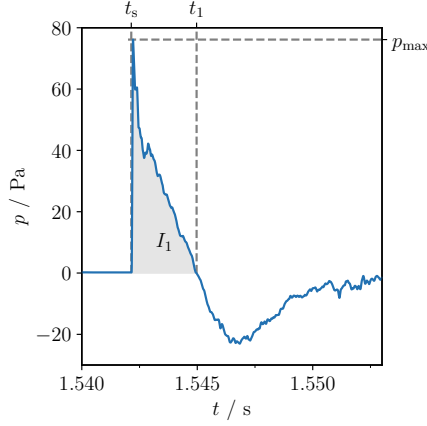
310 The asymmetry of ejecta distribution around the linear charge array is similar to
 311 what was observed in previous off-center multiblast configurations with temporally well
 312 separated charge detonations (Valentine et al., 2015). However, in those experiments a
 313 steep ejecta ring was formed on the side of the crater opposite to the direction of jet in-
 314 clination (Graettinger, Valentine, & Sonder, 2015). This steep ejecta rim was not observed
 315 in the here presented, overlapping blast sequences.

316 The triangular blast sequences of pads 3 and 4 produced more equant crater shapes
 317 resembling blurred circles around the triangular blast centers (Figure 4). Compared to
 318 the linear setups the deepest points of the craters were located laterally closer to the cen-
 319 troid and had a larger distance to the last blast's center. The pad 3 crater had a low point
 320 between the first and second (lateral) blast locations. Pad 4 had the low point close to
 321 its centroid. Both of the craters had shallow slopes near the crater rim, and steeper slopes
 322 closer to the center. Ejecta were concentrated in three main directions for pad 3, and
 323 two for pad 4. Compared to the linear charge setups, the observed ejecta concentrations
 324 of the triangular sequences were less pronounced. The ejecta concentrations originate
 325 from one vertex of the charge configuration to bisect the opposite side of the triangle (sup-
 326 porting video S3). The pad 3 sequence had ejecta concentrations correlating to all three
 327 lateral charge positions. In the pad 4 sequence ejecta rays only correlated to blasts 3, 4
 328 ($\varphi \simeq 150^\circ$) and 5, 6 ($\varphi \simeq 30^\circ$), since the first two blasts occurred in an effectively radi-
 329 ally symmetric setting (blast 1 under flat topography, blast 2 under an approximately
 330 radially symmetric transient cavity).



331

332 **Figure 5:** Ejected mass per area at distances r from the crater center for the four blast
 333 sequences. Blue points show data of a collection branch in the $\varphi = 90^\circ$ -direction. For
 334 pad 1, the other collection branch was at $\varphi = 180^\circ$, which was the main ejection direction.
 335 This branch follows an exponential decay. The 90° -branch follows a power law in all pads.
 336 This branch shows similar decay at higher rates for the linear charge setups in pads 1
 337 and 2 (decays with power $\simeq 3.75 \pm 0.3$), and lower decays rates for the triangular charge
 338 setups in pads 3 and 4 (decays with power $\simeq 3.0 \pm 0.3$).



351

352 **Figure 6:** Typical waveform of a blast pulse as recorded by the acoustic microphones;
 353 here shown is blast #2 of pad 2, at 82 m distance from source (microphone channel 17).
 354 Also shown are characteristic times t_s (shock arrival), t_1 (first zero crossing), maximum
 355 pressure p_{\max} and impulse of the positive pulse part I_1 , that are formulated in Equa-
 356 tions 5 and 6.

358

340

3.3 Seismo-acoustics

341

342

343

344

345

346

The explosion creates a pressure pulse that propagates faster than- or at the speed of sound. Close to the source the pressure jumps (rises discontinuously) from ambient (atmospheric) value to a maximum and then relaxes back before sinking below ambient pressure (Figure 6) and again relaxing back. At larger distances the propagation speed approaches the speed of sound and the pressure discontinuity relaxes to a steep, but finite slope.

347

348

349

350

The recorded data show strong air-to-ground and weak ground-to-air wave coupling. A high-frequency signal occurs in the seismic waveforms in close time correlation with the main blast pulses measured in air at the same location by infrasound and sonic range microphones (Figure 7a–d).

372

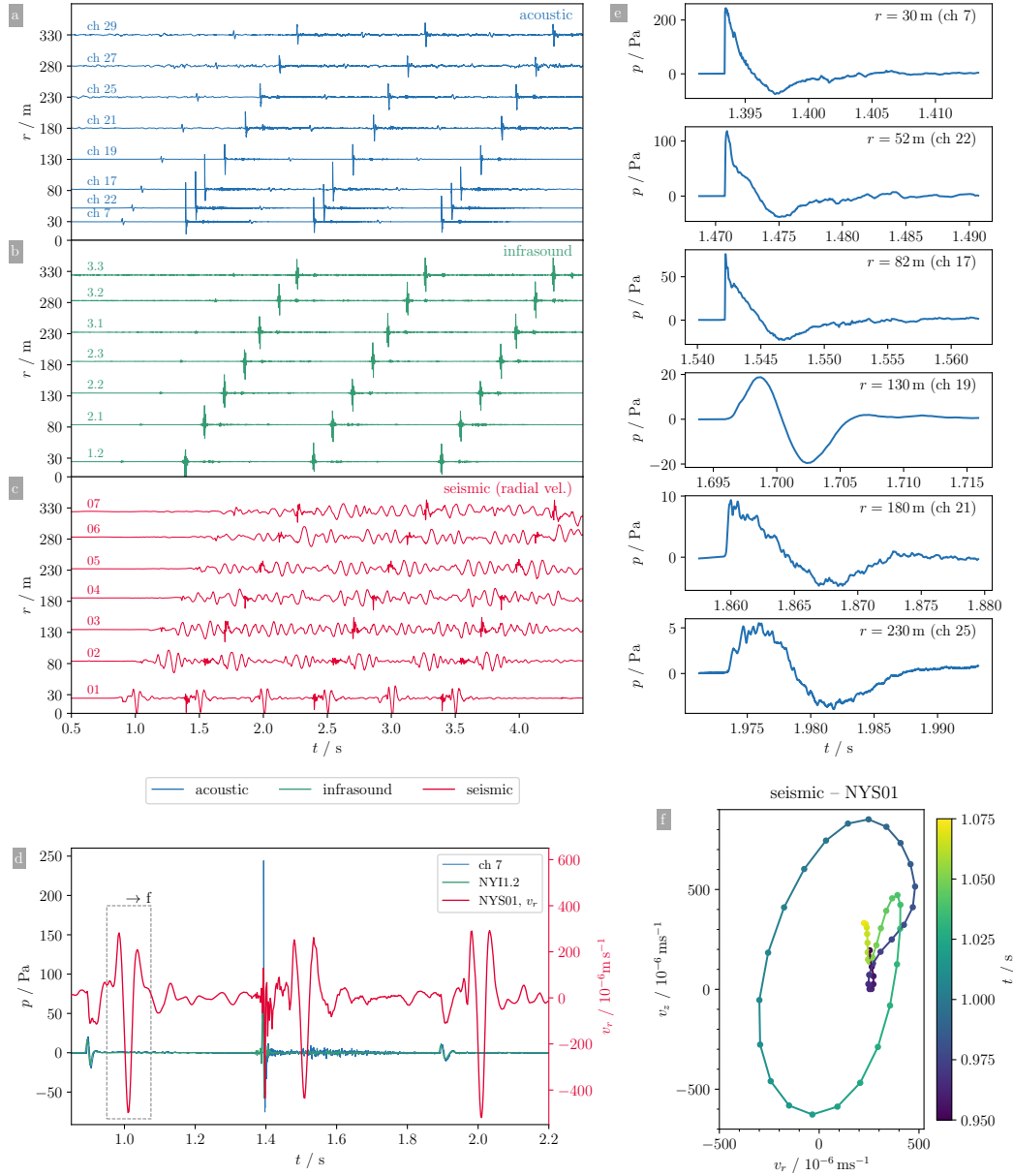
3.3.1 Radial Dependency of Airborne Blast Pulse

373

374

375

Using features of wave-forms recorded by microphones and/or seismic sensors it is possible to estimate the blast's energy, provided that scaling laws assumed in such models are valid. The scaled peak pressure and scaled impulse of a blast in air depends on



359

360 **Figure 7:** Seismic- infrasound- and acoustic waveform signals of the pad 2 blast se-
 361 quence. **a, b, c:** The seismic signals show high-frequency coupling at time and location of
 362 the large pressure pulses occurrence at the infrasound- and acoustic microphones. **d:** First
 363 three pulses at horizontal distance $r = 30$ m. High amplitude air-borne pressure waves,
 364 such as the acoustic (blue) and infrasound (green) signals at $t \simeq 1.6$ s correlate better with
 365 high frequency signal of the seismic channel compared to lower amplitude pulse signals at
 366 about 1.1 s and 2.2 s. **e:** Waveforms of microphone records of blast #2 show a clear tran-
 367 sition at distance < 130 m. The 130 m station recorded a more symmetric signal, while at
 368 180 m the rising slope was steeper (asymmetric) again. **f:** Particle motion of the incoming
 369 Rayleigh wave created by blast #1. The time window picked for the radial and vertical
 370 components is indicated by the dashed rectangle in d.

376 the scaled distance where the pressure is measured (Kinney & Graham, 1985). This re-
 377 lationship can be used to determine the scaled distance of each microphone record, and
 378 with that the energy of each blast wave can be estimated. This resource will be used as
 379 a reference model, and referred to as KG85 data (or -model). For these blasts in air, the
 380 main fundamental three quantities to be scaled are distance, time, and pressure. As in
 381 the case for underground blasts distances can be scaled with blast energy E_b . Addition-
 382 ally, the relatively high atmospheric homogeneity allow further specification of the at-
 383 mospheric density, which is often written in terms of transmission factors for scaled dis-
 384 tance and time. Scaled distance, time, and pressure are given by

$$385 \quad \bar{r} = \frac{f_d r}{E^{1/3}} \quad , \quad \bar{t} = \frac{f_t t}{E^{1/3}} \quad , \quad \bar{p} = \frac{p}{p_a} \quad , \quad (3)$$

386 where p_a is the atmospheric pressure and the transmission factors f_d , f_t for distance and
 387 time, respectively, take the density into account in which the blast pulse propagates. They
 388 are given by

$$389 \quad f_d = \left(\frac{\rho}{\rho_0} \right)^{1/3} = \left(\frac{p_a T_0}{p_0 T} \right)^{1/3} \quad , \quad f_t = \left(\frac{\rho}{\rho_0} \right)^{1/3} \frac{c}{c_0} = \left(\frac{p_a}{p_0} \right)^{1/3} \left(\frac{T}{T_0} \right)^{1/6} \quad . \quad (4)$$

390 The index $_0$ refers to values of a known blast case. The model only applies to explosive
 391 shocks in air. Our recorded pressure pulses show most of the characteristic features of
 392 a free air explosion, indicating that enough energy was not contained in the ground, so
 393 that an estimate of the un-contained energy, E_a , which created a shock pulse in the at-
 394 mosphere, seems appropriate. Comparison to the known yield of the detonation charges,
 395 E_b , can then give information of the effect of explosion depth.

396 Another widely used quantity to measure a blast's intensity, damage potential and
 397 energy is its impulse per crosssectional area (Schnurr et al., 2020; Guzas & Earls, 2010;
 398 Kinney & Graham, 1985; Bush et al., 1946), which can be obtained as the time integral
 399 of the initial positive pressure peak of a microphone pressure curve as

$$400 \quad I_1 = \int_{t_s}^{t_1} p dt \quad . \quad (5)$$

401 Here t_s is the start time (time of arrival of the pulse at the sensor's location) and t_1 is
 402 the time of first zero crossing of the pressure curve (Figure 6). This time interval always
 403 contains the peak pressure. The corresponding scaled impulse is a compound of scaled

404 pressure and time components

$$405 \quad \bar{I}_1 = \int_{\bar{t}_s}^{\bar{t}_1} \bar{p} d\bar{t} = \frac{f_t}{p_a E_b^{1/3}} I_1 \quad . \quad (6)$$

406 The KG85 data provides values up to a scaled distance of $3.1 \text{ m J}^{-1/3}$ ($500 \text{ m kg}^{-1/3}$).
 407 According to this dataset the scaled pressure and scaled impulse decay with $1/\bar{r}$ at relatively large distances ($\bar{r} \gtrsim 10^{-2} \text{ m J}^{-1/3}$, $20 \text{ m kg}^{-1/3}$). The explicit values for the decay are
 409

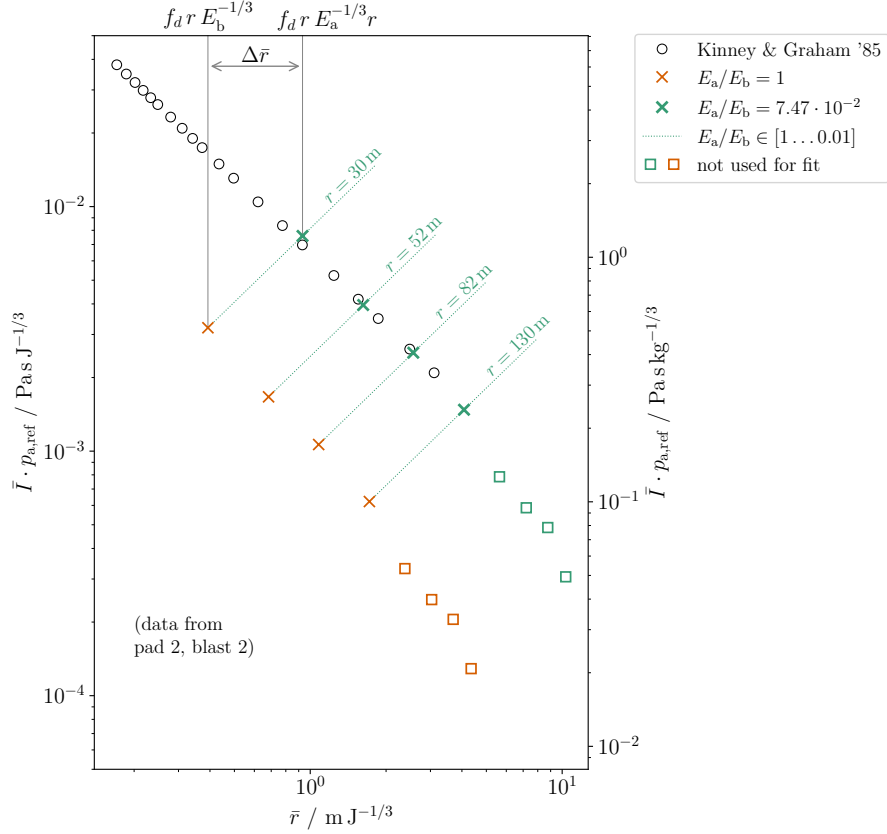
$$410 \quad \bar{p} = \frac{a_{p,\text{ref}}}{\bar{r}} \quad , \quad a_{p,\text{ref}} = 5.135 \times 10^{-3} \text{ m J}^{-1/3} \quad , \quad (7)$$

$$411 \quad \bar{I}_1 = \frac{a_{I,\text{ref}}}{\bar{r}} \quad , \quad a_{I,\text{ref}} = 5.923 \times 10^{-8} \text{ m s J}^{-2/3} \quad . \quad (8)$$

413 As is common in the analysis of blast waves (Garces, 2018; Kinney & Graham, 1985),
 414 peak pressures were not directly read as the maximum of the measured pressure curve,
 415 but impulse I_1 was calculated and compared to a function representing a blast pulse shape.
 416 We used a modified Friedlander shape $\bar{p}(t) = \bar{p}_p (1 - \frac{t-t_s}{t_1-t_s}) \exp(-\alpha \frac{t-t_s}{t_1-t_s})$, see e.g. Marchetti
 417 et al. (2013). The value of p_p that fits the measured I_1 best was used for the peak over-
 418 pressure. The impulse reference data are somewhat unclear, since the given interpolation
 419 function (Appendix B) deviates from the given data points by 17%. The propor-
 420 tionality constant $a_{I,\text{ref}}$ in Equation 8 is a modified value that takes this into account
 421 and is a better fit to the provided reference data.

422 The more contained blasts did not create large enough blast pulses to make a rea-
 423 sonable comparison with the KG85 reference data. However, all initial and the perceived
 424 louder blasts of pads 2 and 4 (blasts 2, 4, 6) created wave forms that were consistent with
 425 blast pulses and could be compared. In those cases peak pressure data were in agree-
 426 ment with a $1/r$ dependency at distances of up to 100 m. The impulse data stay con-
 427 sistent up to about 130 m distance (Figure 9a and b). At larger distances the values de-
 428 viate significantly from $1/r$.

429 To compare the measured impulse values to the scaled reference, an r^{-1} dependency
 430 was fitted to the un-scaled values of a given blast pulse, and the fitting constant a_I was
 431 used to determine the location in the scaled graph. This determines an energy, E_a (“at-



433

434 **Figure 8:** Effect of blast confinement illustrated by a scaled impulse vs. scaled distance
 435 plot. Straight forward calculation of scaled distance using the blast’s total energy E_b puts
 436 the measured scaled impulse (red markers) below the reference values (black circles). The
 437 fitting procedure moves the measured values along the green lines. Since both, impulse
 438 and distance scale with $E^{-1/3}$ their scaled values increase if E decreases. Green markers
 439 show values for minimum deviation from reference which correspond to energy E_a .

441

432 mospheric energy”), that creates the pressure pulse:

$$\begin{aligned}
 \bar{I} &= \frac{a_{I,\text{ref}}}{\bar{r}} = \frac{a_{I,\text{ref}} E_a^{1/3}}{f_d r} \\
 &= \frac{f_t}{p_a E_a^{1/3}} I = \frac{f_t}{p_a E_a^{1/3}} \frac{a_I}{r}
 \end{aligned} \tag{9}$$

$$E_a = \left(\frac{f_d f_t}{p_a} \frac{a_I}{a_{I,\text{ref}}} \right)^{3/2} \tag{10}$$

442

443 Since both, distance and impulse scale with $E_a^{1/3}$, the procedure ‘moves’ values on
 either axis when changing energy (Figure 8). The result are scaled distances at the end

444 of the KG85 reference scale ($\bar{r} \gtrsim 0.6 \text{ m J}^{-1/3}$, $100 \text{ m kg}^{-1/3}$). From the scaled distance \bar{r}
 445 a real distance r corresponds to the energy $E_a = (r/\bar{r})^3$, which can be interpreted as the
 446 energy not contained in the ground, and is smaller compared to the blast energy E_b . E_a
 447 was found to be around 1.5% of E_b for the initial blasts, and about 5–7.5% of E_b for the
 448 loud blasts in pads 2 and 4 (Figure 9c and d, Table 3).

449 Ford et al. (2014) determined distance- and depth dependent energy partitioning
 450 of explosions above and below ground using a model for the airborne signal that, after
 451 some re-formulation (Appendix C), can be written as

$$\bar{I}_1 = \frac{b_1}{\bar{r}} \frac{e^{-\bar{d}/\bar{d}_3}}{(1 + e^{-10\bar{d}/\bar{d}_3})^{1/10}} \quad (11)$$

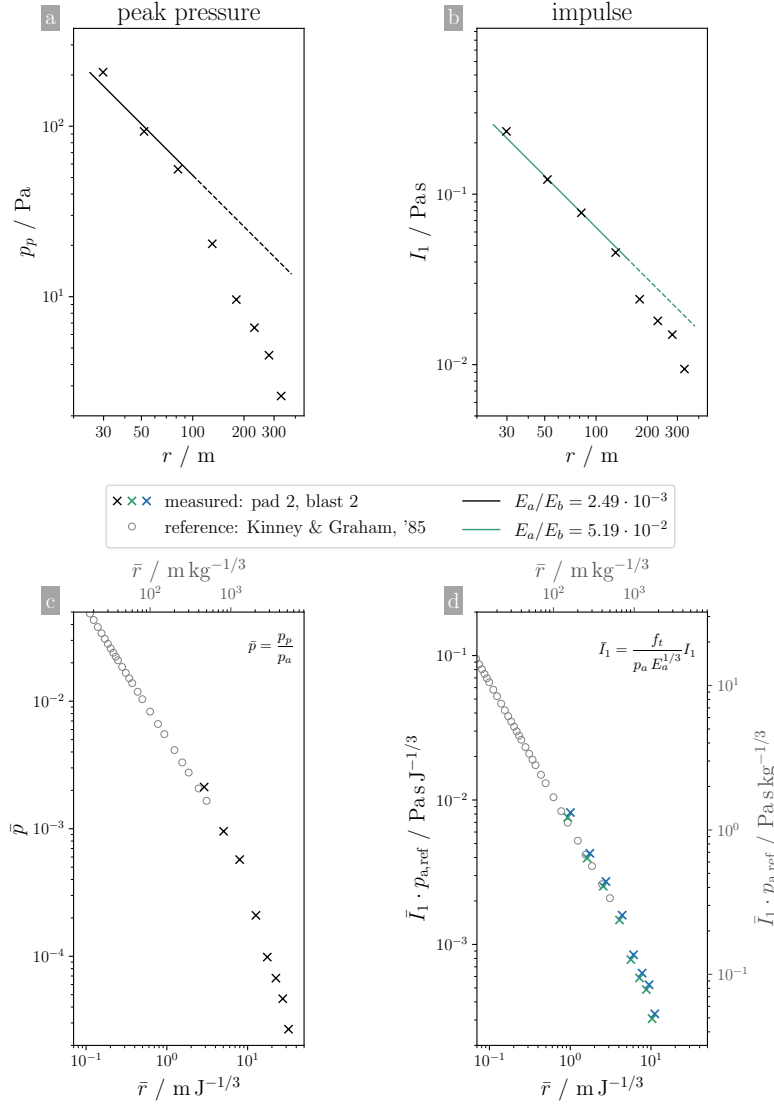
452 Here $b_1 = 1.15 \times 10^{-7} \text{ s m J}^{-2/3}$ and $\bar{d}_3 = 1.2 \times 10^{-3} \text{ m J}^{-1/3}$. Evaluated at $\bar{d} = 0$
 453 this model expects a ca. 7% smaller scaled impulse (factor $2^{-1/10}$, $\simeq 0.93$) at a given
 454 distance compared to a free air blast. A larger discrepancy exists with respect to the KG85
 455 data: The two constants for the \bar{r}^{-1} dependency, $a_{I,\text{ref}}$, b_1 differ by a factor 0.51. Eval-
 456 uating equation 10 using b_1 instead of $a_{I,\text{ref}}$ yields a factor $(a_{I,\text{ref}}/b_1)^{3/2} \simeq 0.37$ reduced
 457 values for E_a . The dataset presented here does not contain a zero depth or free air blast,
 458 and therefore cannot decide for one of the models. Energy values listed in Table 3 used
 459 the KG85 constant, and should be adjusted if used in connection with Equation 11.

481 **3.3.2 Blast Energy, Charge Depth and Explosion Sequence**

482 Equation 11 and microphone records of previous blast sessions, carried out in very
 483 similar host materials and with similar explosives, show that scaled impulse decays rapidly
 484 with scaled depth (Appendix A). A somewhat more accurate match with experimental
 485 data is obtained for the peak pressure dependency on depth. Therefore the following is
 486 formulated using a peak pressure dependency. At depths $\bar{d} < 5 \times 10^{-3} \text{ m J}^{-1/3}$ peak pres-
 487 sure can be approximated by a product of an exponential which contains the depth part
 488 and an amplitude containing the radial dependency:

$$489 \quad p_p = A(\bar{r}) e^{-\bar{d}/\bar{d}_0} \quad (12)$$

490 Here the scaled depth related constant $\bar{d}_0 = 5.4 \times 10^{-4} \text{ m J}^{-1/3}$. This approximation is
 491 valid for scaled depths smaller than $5 \times 10^{-3} \text{ m J}^{-1/3}$ (Figure A1).



460

Figure 9: Comparison of peak pressure p_p and impulse I_1 with respect to their applicability to estimate an explosion energy, and their compatibility to the scaled air blast data by Kinney & Graham, 1985 (KG85). **a, b:** The impulse data show a better agreement with the r^{-1} -trend. Energies E_a estimated from peak pressures are about a factor 10 smaller compared to the impulse-based estimates. The p_p -values start to deviate significantly from the r^{-1} -trend at distances $r > 100$ m. The impulse values start deviating for distances $r > 150$ m. **c:** Only the largest blasts produced scaled peak pressures that are comparable to the KG85 values. **d:** Scaled impulse values show a larger overlap with KG85. This is partially caused by the larger energy estimates, which reduce the scaled impulse *and* the scaled radius.

472 **Table 3:** Results of the acoustic signal analysis: Acoustic energy, E_a , its part of total
 473 blast energy, and reduced depths for all experiments. Only signals from the radial mi-
 474 crophone line were used. All E_a values were derived from a fit to the impulse-distance
 475 relationship (Equations 6 and 8). Only I_1 -values that followed an r^{-1} -dependency were
 476 used for the fit (Figure 9). For the loud blasts of pads 2 and 4 (blasts 2, 4, 6) the r^{-1}
 477 dependency ended for $r > 130$ m. which was the case for microphones at distances up to
 478 130 m ($\bar{r} \leq 1.71 \text{ m J}^{-1/3}$, $276 \text{ m kg}^{-1/3}$).

| Pad | Blast | mics used ¹ | Distance range ² (m) | E_a $\times 10^3 \text{ J}$ | E_a/E_b % | d_{red} | \bar{d}_{red} $\times 10^{-3} \text{ m J}^{-1/3}$ |
|-----|-------|---------------------------|------------------------------------|----------------------------------|-----------------|------------------|---|
| 1 | 1 | 6 | 31.2–280 | 4.32 ± 0.52 | 0.99 ± 0.12 | 0.30 | 3.95 |
| | 3 | 6 | 31.2–280 | 3.88 ± 0.51 | 0.89 ± 0.12 | 0.30 | 3.95 |
| | 2 | 6 | 31.2–280 | 4.48 ± 0.80 | 1.03 ± 0.18 | 0.30 | 3.95 |
| | 4 | 4 | 31.2–280 | 1.71 ± 0.11 | 0.39 ± 0.02 | 0.36 | 4.72 |
| | 5 | 3 | 31.2–280 | 2.59 ± 0.25 | 0.59 ± 0.06 | 0.32 | 4.21 |
| | 6 | 3 | 31.2–280 | 1.11 ± 0.06 | 0.25 ± 0.01 | 0.35 | 4.62 |
| 2 | 1 | 8 | 29.8–330 | 7.92 ± 0.49 | 1.81 ± 0.11 | 0.30 | 3.95 |
| | 2 | 4 | 29.8–130 | 32.62 ± 1.61 | 7.47 ± 0.37 | 0.20 | 2.67 |
| | 3 | – | – | – | – | 0.30 | 3.95 |
| | 4 | 4 | 29.8–130 | 33.37 ± 0.67 | 7.64 ± 0.15 | 0.17 | 2.30 |
| | 5 | 7 | 29.8–330 | 3.62 ± 0.44 | 0.83 ± 0.10 | 0.30 | 3.95 |
| | 6 | 4 | 29.8–130 | 28.92 ± 1.62 | 6.62 ± 0.37 | 0.19 | 2.44 |
| 3 | 1 | 6 | 28.1–280 | 6.17 ± 1.39 | 1.41 ± 0.32 | 0.30 | 3.95 |
| | 2 | 6 | 28.1–280 | 6.28 ± 0.91 | 1.44 ± 0.21 | 0.30 | 3.95 |
| | 3 | 6 | 28.1–280 | 16.10 ± 1.83 | 3.69 ± 0.42 | 0.30 | 3.95 |
| | 4 | 3 | 28.1–80.7 | 3.13 ± 0.24 | 0.72 ± 0.06 | 0.33 | 4.33 |
| | 5 | 5 | 28.1–280 | 6.79 ± 0.68 | 1.56 ± 0.16 | 0.30 | 4.00 |
| | 6 | 3 | 28.1–80.7 | 4.41 ± 0.30 | 1.01 ± 0.18 | 0.07 | 5.05 |
| 4 | 1 | 4 | 48.6–180 | 5.82 ± 0.61 | 1.33 ± 0.14 | 0.30 | 3.95 |
| | 2 | 3 | 48.6–130 | 23.63 ± 0.79 | 5.41 ± 0.18 | 0.22 | 2.91 |
| | 3 | 4 | 48.6–180 | 3.66 ± 0.37 | 0.84 ± 0.08 | 0.30 | 3.95 |
| | 4 | 3 | 48.6–130 | 25.21 ± 0.96 | 5.78 ± 0.22 | 0.22 | 2.93 |
| | 5 | 4 | 48.6–180 | 6.39 ± 0.31 | 1.46 ± 0.07 | 0.30 | 3.95 |
| | 6 | 3 | 48.6–130 | 28.80 ± 1.10 | 6.60 ± 0.25 | 0.24 | 3.22 |

¹: Number of microphones used to fit the radial dependency to the data.

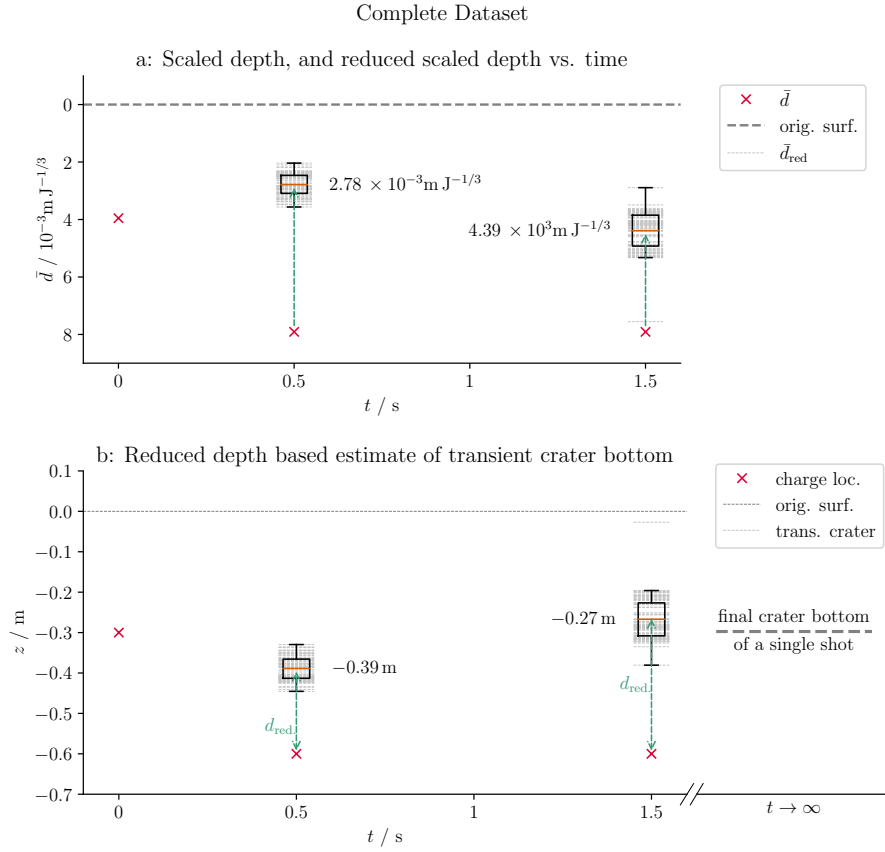
²: Minimum and maximum distance of the microphones used to determine E_a .

492 The first charge of a blast sequence detonated under a flat surface in unaltered host
 493 material. The following charges detonated under changed topography and somewhat al-
 494 tered host material, since their lateral spacing (0.6 m , $8 \times 10^{-3} \text{ m J}^{-1/3}$) corresponds ap-
 495 proximately to the maximum crater radius for that blast energy, and similarly, the ver-
 496 tical spacing (0.3 m , $4 \times 10^{-3} \text{ m J}^{-1/3}$) had, approximately, the optimum depth. Previ-
 497 ous experiments showed that for such scaled distances the blast's jet changes shape and,
 498 if the topography above the charge has an overall orientation, it will also change direc-
 499 tion (Valentine et al., 2015; Ross et al., 2013). If the pre-blast topography is known, parts
 500 of the altered surface morphology can be accounted for by the use of an effective scaled
 501 depth (Sonder et al., 2015). In case of 0.5 s blasting delays the topography is however
 502 not known. However, the Sonder et al. (2015) analysis also shows that an effective ex-
 503 plosion depth rarely deviates by more than 10–20% from the distance to the closest point
 504 to the surface, which is typically the crater bottom. With this approximation, i.e. ne-
 505 glecting the crater shape but not its depth, it is possible to evaluate Equation 12 for peak
 506 pressures of blasts that were shot at same lateral location for the two different blast de-
 507 lays, 0.5 s and 1.5 s that were realized.

508 For the pad 1 and 3 experiments this applies to the following pairs of blasts: (1, 4),
 509 (2, 5), and (3, 6). For the pad 2 and 4 experiments the blast pairs with same lateral lo-
 510 cation are (1, 2), (3, 4) and (5, 6). Evaluating Equation 12 for two peak pressures at same
 511 scaled distance leaves only the scaled depth to change. For example, considering the ra-
 512 tio of peak pressures of pad 2's blasts 2 and 1 relates the scaled depth of blast 2 to the
 513 previous one by

$$\bar{d}_{2,r} = \bar{d}_1 - \bar{d}_0 \ln \frac{p_{p,2}}{p_{p,1}} \quad . \quad (13)$$

514 This formula can be applied to any of the above listed blast couples with consistent re-
 515 sults (Figure 10a), showing that the so-derived depths are reduced by a factor 1.5–3, com-
 516 pared to their initial charge location relative to the surface. Since E_b was the same for
 517 all blasts, the lower charge at the moment of its detonation can be estimated to be at
 518 a depth $d_r = \bar{d}_r E_b^{1/3}$ below the crater bottom at that time. And because the location of
 519 the lower charge is known to be 0.6 m below the original surface, the crater bottom can
 520 be estimated at $z_{\text{bottom}} = -0.6 \text{ m} + d_r$ (Figure 10b). The two delay times show that 0.5 s
 521 after detonation the crater bottom is deeper than at 1.5 s. At 1.5 s the crater bottom is
 522 about the same location that would be expected from a blast of energy E_b at optimum
 523 depth.
 524



525

526 **Figure 10:** Scaled charge depths (blue crosses), reduced scaled depths (gray, dashed
 527 lines: values of a single microphone, orange: average of all microphones) of all microphone
 528 sensors at one angle, plotted against time after detonation of the previous charge located
 529 vertically above. a: At 0.5 s delay, scaled depth is reduced by a factor 2–3 compared to
 530 original charge location. At 1.5 s delay scaled depth is only reduced by a factor 1.5–2. (b)
 531 Estimated of the time dependent crater bottom evolution. For comparison the dashed
 532 gray line shows the measured depth of a single shot of same charge type and energy.

| Pad | Measured Footprint | | Reduced Footprint | | Max. Footprint | |
|-----|------------------------|-------------|------------------------|-------------|------------------------|-------------|
| | Area m ² | Radius m | Area m ² | Radius m | Area m ² | Radius m |
| 1 | 3.71 | 0.78 | 3.97 | 0.81 | 4.26 | 0.85 |
| 2 | 3.38 | 0.73 | 3.73 | 0.78 | 4.26 | 0.85 |
| 3 | 2.79 | 0.68 | 3.76 | 0.83 | 3.92 | 0.85 |
| 4 | 3.13 | 0.73 | 3.71 | 0.82 | 3.92 | 0.85 |

Table 4: Measured-, reduced- and maximum expected crater sizes for the tested explosion configurations. The reduced footprint is the maximum possible footprint when blasting at the reduced depth. The maximum footprint is the overall maximum that can be expected from the given blast energy.

3.3.3 Seismic Signal

We present here an initial estimate of seismic energy involved in the explosion experiments. A deep analysis of the seismic records will be part of future studies. The energy radiated from a radially symmetric seismic source may be estimated from the measured square velocity of the ground (particle) motion u_r (e.g. Boatwright, 1980; Johnson & Aster, 2005)

$$E_s = 2\pi r^2 \frac{\rho_g c_g}{A} \int_0^{\infty} S u_r^2(r, t) dt \quad . \quad (14)$$

Here A and S are coefficients for signal attenuation and site response, respectively. ρ_g is the ground density and c_g the propagation speed of the ground, both at the observation location. For this first broad look at seismic energy these parameters are assumed to be constant. In this assumed energy estimate only one component of ground motion, radial component u_r is non-zero. Other seismic components are therefore ignored in the following. Then E_s can be approximated as

$$E_s \simeq F r^2 \int_0^{\infty} u_r^2(r, t) dt \quad , \quad F = 2\pi \rho_g c_g \frac{S}{A} \quad . \quad (15)$$

In this approximation the proportionality factor F depends on a combination of ground properties and attenuation characteristics, but not on E_s .

555 The multi-blast setting adds the difficulty that seismic signals originating from dif-
 556 ferent blasts overlap at larger distances (e.g. for $r \gtrsim 80$ m, Figure 7c). From such distances
 557 only the cumulative seismic energy of a blast set can be determined:

$$\sum_{i=0}^{N_b} E_{s,i} = F r^2 \int_0^{\infty} u_r^2(r, t) dt \quad (\text{here } N_b = 6). \quad (16)$$

558 At closer ranges the blasts can be identified clearly in the u^2 signal. There u^2 decays quickly
 559 before the next pulse arrives, and integration over a finite time interval is a valid approx-
 560 imation for each blast (Figure 11a):

$$E_{s,i} = F r^2 \int_{\Delta t_i} u_r^2(r, t) dt \quad (17)$$

588 When compared to the airborne signals, the seismic records show an inverted trend:
 589 The “muffled” blasts 1, 3 and 5 of pads 2 and 4, which had a much lower airborne sig-
 590 nal created a larger seismic signal, when compared to blasts 2, 4 and 6 (Figure reffig:seisa).
 591 This behavior serves as motivation for a potential energy partitioning scheme. For a given
 592 pad configuration the assumption is made that seismic and acoustic energy of a blast add
 593 up to a constant value.

$$E_b = E_a + E_s + E_{\text{rem}} \quad (18)$$

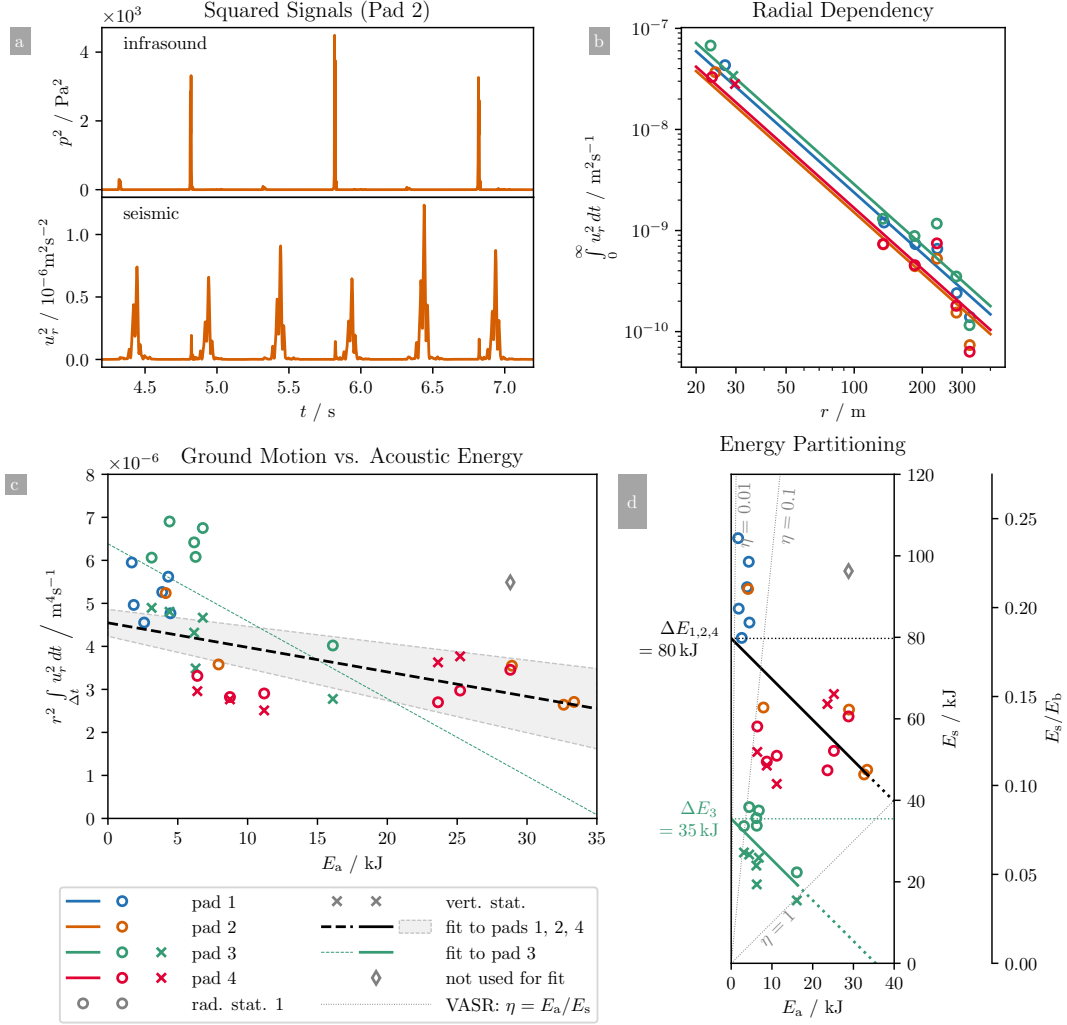
594 In this picture a change in E_a of δE , for example by a change of blast depth, would re-
 595 sult in a change of E_s by $-\delta E$. The remaining energy E_{rem} stays constant. This energy
 596 conservation applies to each blast and to the cumulative case, which allow determina-
 597 tion of the two unknowns F and E_{rem} . With $\Delta E = E_b - E_{\text{rem}}$ the per-blast case be-
 598 comes

$$r^2 \int_{\Delta t_i} u_r^2(r, t) dt = \frac{E_{s,i}}{F} = \frac{\Delta E - E_{a,i}}{F} \quad , \quad (19)$$

599 and the cumulative case is

$$\begin{aligned} \int_0^{\infty} u_r^2(r, t) dt &= \frac{N_b E_b - N_b E_{\text{rem}} - \sum E_{a,i}}{F r^2} \\ &= N_b \frac{\Delta E - \langle E_a \rangle}{F r^2} \quad , \end{aligned} \quad (20)$$

600 where $\langle E_a \rangle = \sum E_{a,i} / N_b$. The difference between the two cases is that for Equation 20
 601 r is treated as independent variable, while in Equation 19 E_a is independent. The av-
 602 erage value $\langle E_a \rangle$ is a constant.



561

Figure 11: Estimate of seismic energy from squared particle velocity. **a:** Pad 2 test squared pressure signal of the infrasound sensor and squared particle velocity at first radial station (30 m distance). The seismic signal shows clearly identifiable pulses that can be separated into six time intervals. As described earlier for pad 2 the airborne pressure pulses of blasts 1, 3 and 5 are much weaker as those of blasts 2, 4 and 6. In contrast peak values of u^2 are higher for blasts 1, 3 and 5, and somewhat weaker for blasts 2, 4 and 6. The trend is not as strong for the seismic signal as it is for the airborne signal. **b:** Radial dependency of squared particle velocity integral. Measured values and fitted r^{-2} curves of Equation 20 are shown. Pads 1 and 3, with sequential shot depth configuration, produced a higher squared particle velocity integral, compared to pads 2 and 4 (interchanging shot depth). To a lesser degree, the triangular pads 3, and 4 had larger values when compared to the same shot depth configuration of the linear geometrical setups of pads 1, and 2. **c:** Squared particle velocity integral dependency on E_a . Despite some scatter, data from pads 1, 2 and 4 follow a common trend, while pad 3 data has a larger slope and offset.

576

578 **Figure 11:** [*Continued*] The black dashed line is a fit of Equation 19 to data of pads 1,
 579 2, and 4. The green dotted line to the pad 3 data. Cross markers show data from ra-
 580 dial station#1, circles data from the vertical station. **d:** Seismic energy plotted against
 581 acoustic energy for all pads. Black and green lines show the anticipated (linear) relation-
 582 ships using the derived values for F and ΔE . The second vertical axis shows E_s relative
 583 to total blast energy E_b . The elastic part is ca. 17% of E_b for pads 1, 2, 4 and ca. 10%
 584 for pad 3. Gray dotted lines show the volcanic acoustic seismic ratio $\eta = E_a/E_s$ (VASR,
 585 Johnson & Aster, 2005). The blasts had VASR values between 10^{-2} and 1.
 586

587

603 The left hand side values of Equation 20 were fitted to an r^{-2} dependency. The
 604 result shows the expected behavior: Pads 2 and 4 with the large airborne signals have
 605 smaller seismic signals when compared to their respective geometric counterparts pads 1
 606 and 3 (Figure 11b). The per-blast data for the right-hand side of Equation 19 show a
 607 different trend of the pad 3 data compared to the other pads (Figure 11c). For small E_a
 608 they are larger than the other pads, and then fall off quicker with rising E_a . Since for
 609 the other pads no unique trend could be determined, pad 3 was treated separately, form
 610 pads 1, 2 and 4. For both cases intercept and slope were determined. Together with the
 611 cumulative case fit, values for ΔE and F were calculated. For pads 1, 2 and 4, ΔE about
 612 17% of E_b ($\simeq 73$ kJ), for pad 3 this value is about 10% ($\simeq 45$ kJ). Highest values of E_s
 613 are a factor two larger than highest values of E_a . Consequentially in cases of observed
 614 higher E_a blasts, seismic and airborne energies were comparable (Figure 11d). To be com-
 615 plete, values for F are 3.5×10^9 Js m $^{-4}$ for pads 1, 2, 4, and 1.6×10^9 Js m $^{-4}$ for pad 3.

616 4 Discussion

617 Any number of subsurface explosions at given lateral location create crater struc-
 618 tures (“multiblast craters”) of a limited size, determined by the explosion’s energy, be-
 619 cause any single explosion can eject material only to a finite distance (Sonder et al., 2015).
 620 Accordingly, the sizes of the presented craters are larger than one-blast craters, but smaller
 621 than they could become when blasting many times at these lateral locations with the
 622 same energy. Overlapping footprints from laterally shifting, time separated explosions
 623 create compound craters with a footprint area that can be calculated from overlapping

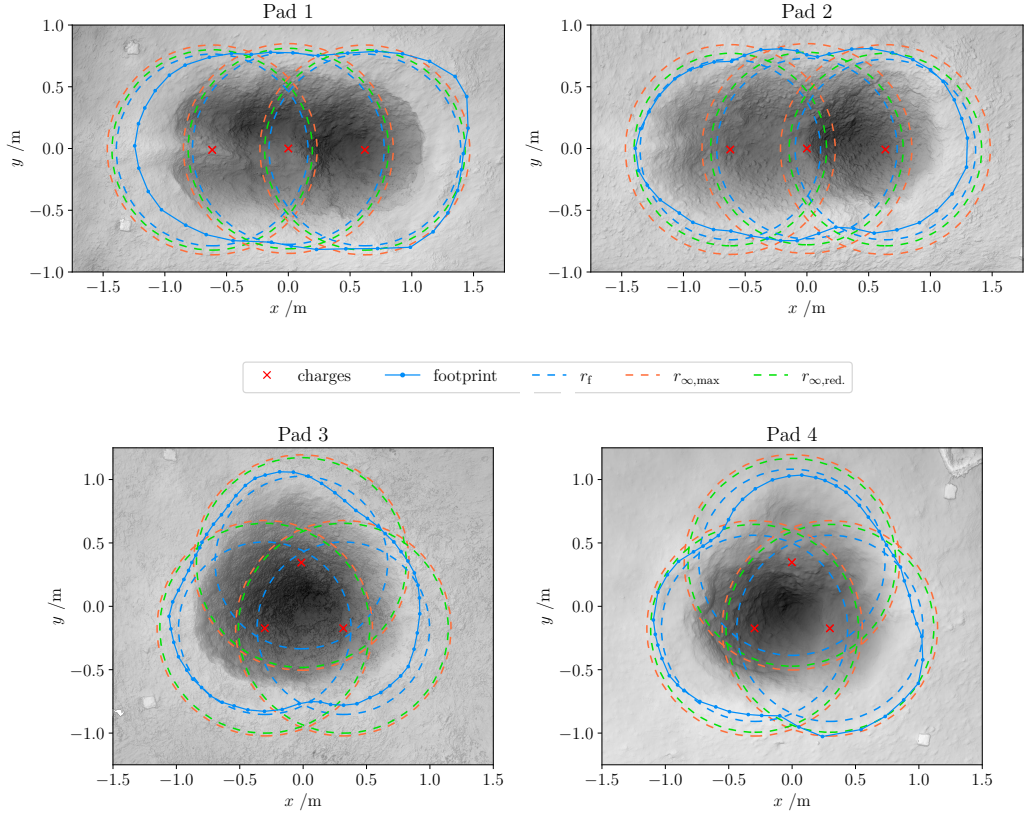
624 circles centered around blast locations (Valentine et al., 2015). For a given explosion depth
 625 a radius is related to explosion energy by the scaled radius, and therefore the footprint
 626 area is, too. The maximum crater radius that can be realized with many explosions of
 627 a given energy is related to the crater radius of one explosion by

$$r_{\infty, \max} = \frac{r_{1, \max}}{1 - e^{-1/n_0}} \simeq 1.49 \bar{r}_{1, \max} E_b^{1/3} = 0.85 \text{ m} \quad , \quad (21)$$

628 where $n_0 = 0.9$ is an experimentally determined constant, and $\bar{r}_{1, \max} = 7.5 \times 10^{-3} \text{ m J}^{-1/3}$
 629 is the maximum scaled radius of one explosion, which occurs at the optimum scaled depth
 630 (Sonder et al., 2015). The footprint radii measure in this study fit into this picture: they
 631 range between 0.68 m and 0.78 m, which is larger than the single explosion radius (0.57 m)
 632 and smaller than the many-blasts limit. However, the crater sizes are not consistent with
 633 respect to the blasting sequence: in case of the linear setup, pad 1 (upper before lower
 634 charges) created a larger crater compared to pad 2 (interchanging charge depths), while
 635 in case of the triangular setup pad 4 (interchanging depths) created the larger crater when
 636 compared to pad 3 (Table 4).

637 Equation 21 can also be used to estimate the final crater size of a hypothetical crater
 638 that would be the result of many blasts at reduced depth. It is then necessary to replace
 639 the maximum (scaled) crater radius with the reduced radius. The latter can be calcu-
 640 lated from the scaled depth dependency, using the scaled reduced depth value. A foot-
 641 print size estimated this way is larger than the measured two-blast crater, and ca. 7%
 642 smaller compared to the maximum possible crater (Table 4, Figure 12).

652 Determination of the atmospheric energy E_a from airborne impulse or peak pres-
 653 sure is possible for scaled distances up to about $5 \text{ m J}^{-1/3}$ ($800 \text{ m kg}^{-1/3}$). At larger dis-
 654 tances this type of analysis yields faulty values. A word of caution must be added, since
 655 the empirical models by Kinney and Graham (1985) and Ford et al. (2014) yield a fac-
 656 tor 2 to 3 different energy estimates. A more in-depth analysis that focuses on the com-
 657 plete seismo-acoustic dataset of the presented experiments may help here. For example,
 658 peak pressure of a weak shock (e.g. Young et al., 2015; Muhlestein et al., 2012; Rogers,
 659 1977) decays with a power of radius slightly larger than 1. Such a dependency may be
 660 observed in the presented data (Figure 9a). Other non-linear acoustic factors and near-
 661 field topography may also play a role (Maher et al., 2020). Nevertheless, both models
 662 evaluated here result in single digit values for the percentage of the energy ratio E_a/E_b .
 663 The relatively small amounts of explosives used, have the advantage that analysis does



643

644 **Figure 12:** Map views of the four craters, their footprints, and footprint equiv-
 645 alent circles of corresponding radii. All radii correspond to an explosion energy,
 646 $E_b = 4.635 \times 10^5$ J. Blue lines represent the measured footprint (topographic high).
 647 Blue dashed circles are the equivalent radii. Green lines represent the maximum possi-
 648 ble footprint that can be expected from this blast energy. Red lines show the hypothet-
 649 ical footprint that would be the result of many explosions at the average reduced depth as
 650 measured in each pad.

664 not have to deal with complications arising from drastically changing transmission fac-
 665 tors (Equation 4), as in the case of large scale explosive events (e.g. Kim & Rodgers, 2016,
 666 2017) or volcanic eruptions (Matoza et al., 2009).

667 The changes in the apparent (“reduced”) crater depth over time show that 0.5 s af-
 668 ter detonation the crater is about a factor 1.5 deeper compared to 1.5 s after detonation.
 669 It is not clear whether this is the time of the transient cavity’s maximum opening or not.
 670 The depth at 1.5 s is comparable to the depth of a single blast crater. For volcanic ac-
 671 tivity the timescale on which a crater forms is important. In this period part of the over-
 672 lying mass confining magma in the ground is reduced, creating an effectively reduced load,
 673 changing- or enabling non-steady state processes, such as magma-water mixing and phreato-
 674 magmatism (Büttner & Zimanowski, 1998; Lorenz, 1975) or decompression driven ac-
 675 tivity (Gonnermann & Manga, 2007). Assuming for a moment without proof that crater
 676 formation duration scales, analog to other blast related time and length (e.g. blast depth,
 677 crater radius), with $E_b^{1/3}$, the presented results mean that for $E_b = 0.4365$ MJ crater
 678 formation lasts on the order of 1 s, which corresponds to a scaled duration of $1.3 \times 10^{-2} \text{ s J}^{-1/3}$.
 679 An event creating a crater of about 15 m diameter would need 10^9 J (Valentine et al.,
 680 2014) if created by a single blast, and would be formed in $1.3 \times 10^{-2} \text{ s J}^{-1/3} \times 10^3 \text{ J}^{1/3} =$
 681 13 s. A 25 m diameter crater would then need 44 s to form. It is, however, likely that other
 682 factors complicate such a straight forward scaling approach.

683 Despite such scaling difficulties the experiments show that explosions which occur
 684 at depths previously thought to be contained in the subsurface (Valentine et al., 2014)
 685 have to be considered potentially hazardous, if there is a realistic probability that it could
 686 occur as a result of crater formation above. The scenario of successively crater deepen-
 687 ing, which is also of military interest (Antoun et al., 2003), cannot repeat indefinitely,
 688 since the following crater needs to move material from greater depth to the surface in
 689 a finite time window, which needs energy. More experiments are necessary to test where
 690 this limit lies, and what the exact crater formation duration is.

691 Analysis of the seismic signal reveals why the pad 3 crater is smaller compared to
 692 pad 4: Pad 3 had different attenuation- and coupling conditions leading to less energy
 693 available for seismic and acoustic pressure or momentum generation (ΔE), and more en-
 694 ergy dissipated without momentum generation. The different coupling is likely the re-
 695 sult of a variation in the pads host properties: On a subjective level, personnel prepar-

696 ing the pad for charge placement before blasting, can confirm that pad 3 ‘felt’ somewhat
 697 different compared to the others when punching holes for charge placement into the ma-
 698 terial. Such unintentional host variability highlights the sensitivity of the crater forma-
 699 tion process to host properties (see also Macorps et al., 2016). The estimate of seismic
 700 energy and the energy partitioning analysis rely on good knowledge of E_a . The assump-
 701 tions made to estimate E_s work well for large values of E_a . At smaller E_a (more con-
 702 tained blasts) scatter becomes larger, which suggests that the underlying assumption,
 703 that energy is partitioned only between seismic and airborne signal producing effects,
 704 does not apply there. The squared velocity- and pressure signals of pads 1 and 3 empha-
 705 size this trend (Supporting Information Figure S9 and Figure 11a). In a first order es-
 706 timate combination of the available data from the blasts in pads 1, 2 and 4 was between
 707 10% and 20% of E_b , and between 5% and 10% for the blasts of pad 3. The experiments
 708 show how explosive energy is contained by friction, strength and inertia of the surround-
 709 ing (overlying) material, and how energy translates from driving ground-bound (seismic)
 710 to airborne processes, once the overarching containment parameter, scaled depth \bar{d} , changes.

711 5 Conclusions

712 Rapidly-timed subsurface blasts, occur in fields such as mining, geotechnical, mil-
 713 itary and medical applications (Qiu et al., 2018; Arora et al., 2017; Zhou et al., 2016; Mam-
 714 madova et al., 2017). Our analysis of the ejecta, crater morphology, and seismo-acoustic
 715 signals should be applicable to those situations. We highlight volcanic eruptions, which
 716 often involve explosions in rapid succession (Dürig, Gudmundsson, Karmann, et al., 2015;
 717 Pistolesi et al., 2011). The results of this study provide insight on how to quantitatively
 718 interpret geophysical signals measured during such eruptions, as well as the resulting craters
 719 and deposits. They show that energy is a robust parameter to relate the transient, dy-
 720 namic phenomena, such as airborne and seismic pressure and stress waves and debris jets,
 721 with the long term products such as crater, subsurface deposits and ejecta. Finally, we
 722 emphasize that much of the presented physical signal analysis relies on (a) the high fre-
 723 quency records of airborne signal and (b) on the combination of relative near-field and
 724 far-field records. Deployment of such sensors hold promise for progress in seismo-acoustic
 725 volcano monitoring.

Appendix A Depth- and Distance Dependency of Peak Pressures from Previous Experiments

In previous blasting experiments (Ross et al., 2013; Graettinger et al., 2014; Valentine et al., 2015; Sonder et al., 2015), a set of uncalibrated microphones was placed every 5 m starting at 5 m to 30 m distance from the source. In all experiments the microphones were placed 10 cm above the ground facing towards the blast center. The blasts happened at various scaled depths with an emphasis roughly around optimum excavation conditions ($\bar{d} \simeq 4 \times 10^{-3} \text{ m J}^{-1/3}$), but also deeper and some shallower blasts. Despite the uncalibrated pressure signal the raw signals were evaluated, since all sensors were of same model and therefore comparable. The result can be used to determine the relative depth dependency of impulse- and pressure signals, and compare them to other work (e.g. Ford et al., 2014). Signals were evaluated for peak pressure and impulse the same way as described for the here presented experiments in the main text.

Results show that the expected exponential depth dependency (Equation 11) underestimates both, pressure and impulse for deeper blasts (Figure A1). Therefore a second term that only depends on scaled distance was added to the combined depth- and distance dependencies

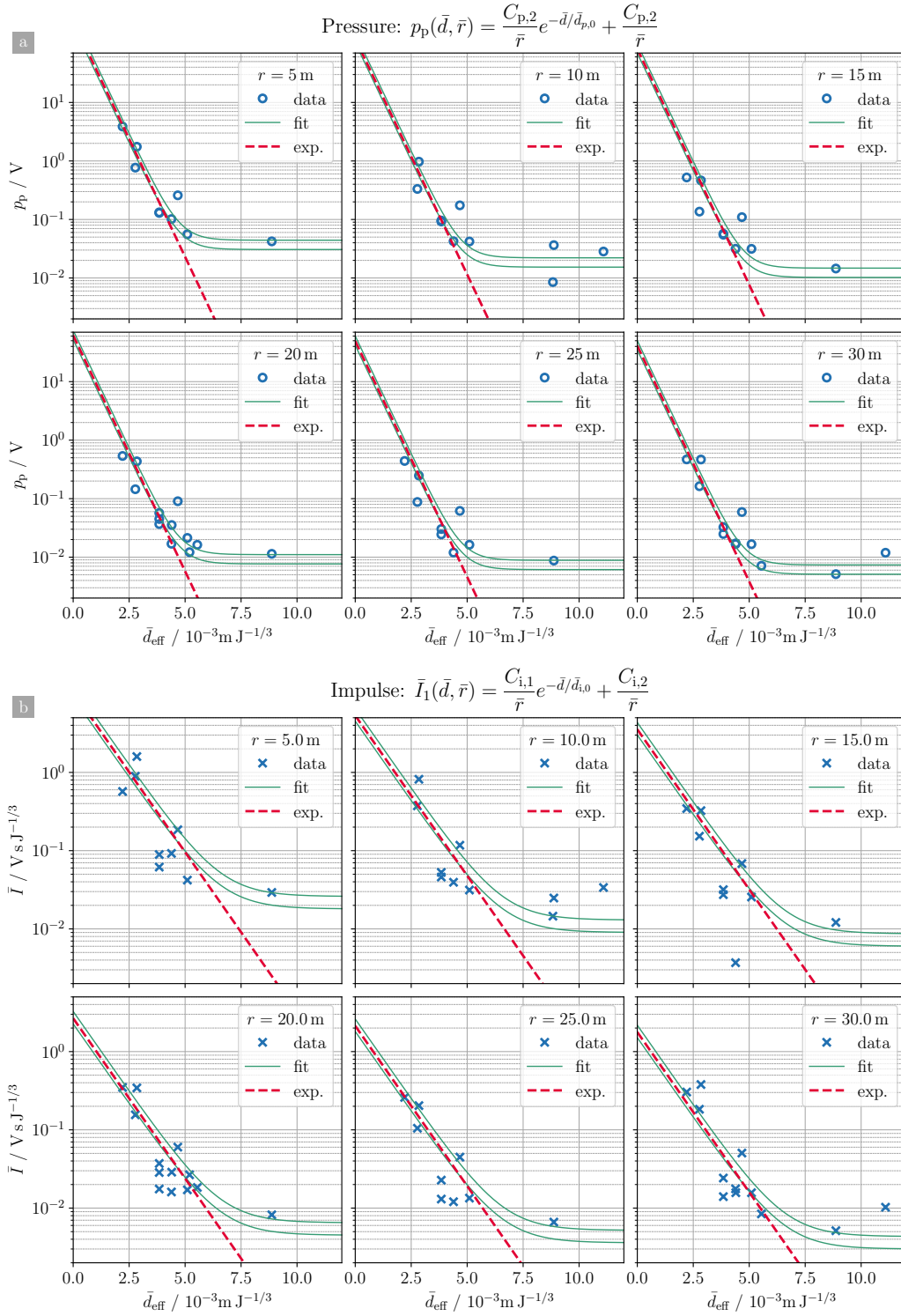
$$p_p(\bar{d}, \bar{r}) = \frac{C_{p,1}}{\bar{r}} e^{-\bar{d}/\bar{d}_{p,0}} + \frac{C_{p,2}}{\bar{r}} \quad , \quad (\text{A1})$$

$$\bar{I}(\bar{d}, \bar{r}) = \frac{C_{i,1}}{\bar{r}} e^{-\bar{d}/\bar{d}_{i,0}} + \frac{C_{i,2}}{\bar{r}} \quad . \quad (\text{A2})$$

At scaled depths smaller than $1.2 \bar{d}_{\text{opt}} (\simeq 5 \times 10^{-3} \text{ m J}^{-1/3})$ the first term dominates, and the peak pressure show an exponential dependency (Figure A1). At larger scaled depths peak pressures decay slower than this exponential predicts. More research is necessary, to clarify the slow decay. Bowman et al. (2014) suggest that ground motion dominates the airborne signal at larger depths. Best fitting values for the depth decay constant in the exponential is for the pressure case $\bar{d}_{p,0} = (5.4 \pm 0.5) \times 10^{-4} \text{ m J}^{-1/3}$, and for the impulse case $\bar{d}_{i,0} = (1.1 \pm 0.3) \times 10^{-3} \text{ m J}^{-1/3}$. $\bar{d}_{i,0}$ deviates by about 12% from the value found by Ford et al. (2014) responsible for depth decay (\bar{d}_3 , Table C1). We interpret this as good agreement for the range $0 \leq \bar{d} \leq 5 \times 10^{-3} \text{ m J}^{-1/3}$.

Appendix B Interpolation Constants of KG85 Pressure and Impulse

The empirical equations for dependencies of blast overpressure, scaled impulse and scaled blast duration on scaled distance are as follows.



755

756 **Figure A1:** Peak pressure (a) and scaled impulse (b) of previous blast experiments,
 757 measured between 5 m and 30 m from the blasts. Pressures are shown in raw units (Volts).
 758 Depth dependencies are exponential for $\bar{d} \leq 5 \times 10^{-3} \text{ m J}^{-1/3}$. [Caption continues...]

760 **Figure A1:** [*Continued*] Peak pressure decays roughly double as fast compared to im-
 761 pulse ($\bar{d}_{p,0} = 5.4 \times 10^{-4} \text{ m J}^{-1/3}$, $\bar{d}_{i,0} = 11 \times 10^{-4} \text{ m J}^{-1/3}$). The red dashed lines are the
 762 exponentials $C_{p,1}e^{-\bar{d}/\bar{d}_{p,0}}/\bar{r}$ and $C_{i,1}e^{-\bar{d}/\bar{d}_{p,0}}/\bar{r}$, for pressure and impulse, respectively.
 764

768 Overpressure:

$$\bar{p} = \bar{p}_0 \frac{1 + \left(\frac{\bar{r}}{Z_{p,0}}\right)^2}{\sqrt{1 + \left(\frac{\bar{r}}{Z_{p,1}}\right)^2} \sqrt{1 + \left(\frac{\bar{r}}{Z_{p,2}}\right)^2} \sqrt{1 + \left(\frac{\bar{r}}{Z_{p,3}}\right)^2}} \quad (\text{B1})$$

769 Scaled impulse:

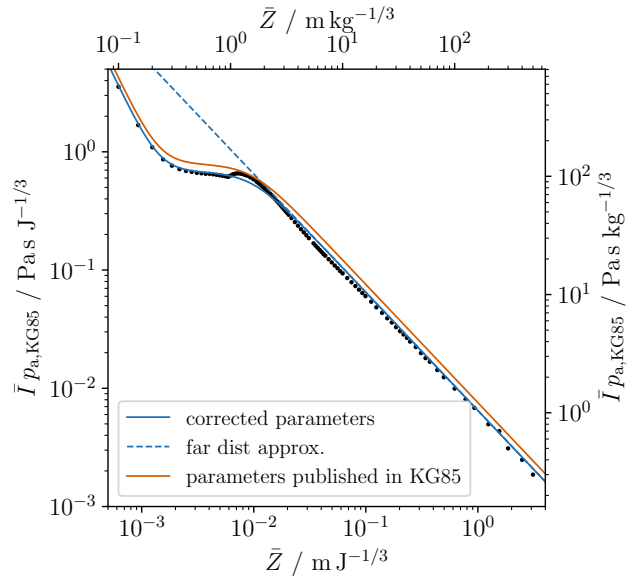
$$\bar{I}_1 = \bar{I}_0 \frac{\sqrt{1 + \left(\frac{\bar{r}}{Z_{I,0}}\right)^4}}{\left(\frac{\bar{r}}{Z_{I,1}}\right)^2 \left(1 + \left(\frac{\bar{r}}{Z_{I,2}}\right)^3\right)^{1/3}} \quad (\text{B2})$$

770 Scaled blast duration:

$$\bar{t}_d = \bar{t}_0 \frac{1 + \left(\frac{\bar{r}}{Z_{t,0}}\right)^{10}}{\left(1 + \left(\frac{\bar{r}}{Z_{t,1}}\right)^3\right) \left(1 + \left(\frac{\bar{r}}{Z_{t,2}}\right)^6\right) \left(1 + \left(\frac{\bar{r}}{Z_{t,3}}\right)^2\right)^{1/2}} \quad (\text{B3})$$

771 Values for the constants $Z_{x,y}$ are given in Table B1. For large distances, i.e. $\bar{r} \gg Z_{x,y}$
 772 the 1 in each of the factors in the above formulas becomes small when compared to the
 773 factor $\bar{r}/Z_{x,y}$ and can be neglected. Then \bar{p} and \bar{I} go with \bar{r}^{-1} :

$$\begin{aligned} \bar{p} &\sim \bar{p}_0 \frac{Z_{p,1}Z_{p,2}Z_{p,3}}{Z_{p,0}} \frac{1}{\bar{r}} = \frac{a_{p,\text{ref}}}{\bar{r}} \\ \bar{I} &\sim \bar{I}_0 \frac{Z_{I,1}^2 Z_{I,2}}{Z_{I,0}^2} \frac{1}{\bar{r}} = \frac{a_{I,\text{ref}}}{\bar{r}} \end{aligned} \quad (\text{B4})$$



774

775 **Figure B1:** Effect of corrected value for \bar{I}_0 on the interpolation curve (Equation B2).

776 For a reason not known to the authors the original value for \bar{I}_0 (orange curve) does not

777 fit the KG85 data (black dots) well. We used a changed value, which better fits this data

778 (blue curves, Table B1).

Table B1: Constants for the empirical interpolation formulas for blast pulse overpressure, scaled impulse and scaled duration, in SI and kg-TNT equivalent units.

| Constant | SI | kg _{TNT} | Remarks |
|-----------------|--|---|---|
| <u>Pressure</u> | | | |
| \bar{p}_0 | 8.08×10^2 | 8.08×10^2 | Scaled length- and time units differ by a factor of the 1/3 power of 1 kg TNT explosive energy. $(E_{\text{kg TNT}})^{1/3} = (4.184 \times 10^6 \text{ J})^{1/3} = 161.1 \text{ J}^{1/3}$. |
| $Z_{p,0}$ | $2.79 \times 10^{-2} \text{ m J}^{-1/3}$ | $4.50 \text{ m kg}^{-1/3}$ | |
| $Z_{p,1}$ | $2.98 \times 10^{-4} \text{ m J}^{-1/3}$ | $4.80 \text{ m kg}^{-1/3}$ | |
| $Z_{p,2}$ | $1.99 \times 10^{-3} \text{ m J}^{-1/3}$ | $0.32 \text{ m kg}^{-1/3}$ | |
| $Z_{p,3}$ | $8.38 \times 10^{-3} \text{ m J}^{-1/3}$ | $1.35 \text{ m kg}^{-1/3}$ | |
| <u>Impulse</u> | | | |
| \bar{I}_0 | $3.52 \times 10^{-7} \text{ s J}^{-1/3}$ | $5.68 \times 10^{-5} \text{ s kg}^{-1/3}$ | Original value for \bar{I}_0 from Kinney and Graham (1985) is $6.61 \times 10^{-5} \text{ s kg}^{-1/3} = 6.7 \times 10^{-2} \text{ bar ms kg}^{-1/3} / 1.01325 \text{ bar}$. |
| $Z_{I,0}$ | $1.43 \times 10^{-3} \text{ m J}^{-1/3}$ | $0.23 \text{ m kg}^{-1/3}$ | |
| $Z_{I,1}$ | $6.21 \times 10^{-3} \text{ m J}^{-1/3}$ | $1.00 \text{ m kg}^{-1/3}$ | |
| $Z_{I,2}$ | $9.62 \times 10^{-3} \text{ m J}^{-1/3}$ | $1.55 \text{ m kg}^{-1/3}$ | |
| <u>Duration</u> | | | |
| \bar{t}_0 | $6.08 \times 10^{-3} \text{ s J}^{-1/3}$ | $0.980 \text{ s kg}^{-1/3}$ | |
| $Z_{t,0}$ | $3.35 \times 10^{-3} \text{ m J}^{-1/3}$ | $0.54 \text{ m kg}^{-1/3}$ | |
| $Z_{t,1}$ | $1.24 \times 10^{-3} \text{ m J}^{-1/3}$ | $0.02 \text{ m kg}^{-1/3}$ | |
| $Z_{t,2}$ | $4.59 \times 10^{-3} \text{ m J}^{-1/3}$ | $0.74 \text{ m kg}^{-1/3}$ | |
| $Z_{t,3}$ | $4.28 \times 10^{-2} \text{ m J}^{-1/3}$ | $6.90 \text{ m kg}^{-1/3}$ | |

Table C1: Constants for the empirical impulse scaling formula from Ford et al., 2014.

| Constant | | SI | kg _{TNT} |
|---------------------|---|---|---|
| β_1 | $b_1 = \frac{1 \text{ Pa s m}}{p_{a,\text{ref}}} \times \frac{10^{\beta_1}}{E_{\text{kg,TNT}}^{2/3}}$ | 2.48 | 2.48 |
| b_1 | | $1.15 \times 10^{-7} \text{ s m J}^{-2/3}$ | $1.85 \times 10^{-5} \text{ s m kg}^{-2/3}$ |
| β_3 | $\bar{d}_3 = \frac{1}{\beta_3 \ln 10}$ | $3.46 \times 10^2 \text{ J}^{1/3} \text{ m}^{-1}$ | $2.15 \text{ kg}^{1/3} \text{ m}^{-1}$ |
| \bar{d}_3 | | $1.25 \times 10^{-3} \text{ m J}^{-1/3}$ | $0.202 \text{ m kg}^{-1/3}$ |
| $p_{a,\text{ref}}$ | | $1.01325 \times 10^5 \text{ Pa}$ | $1.01325 \times 10^5 \text{ Pa}$ |
| $E_{\text{kg,TNT}}$ | | $4.184 \times 10^6 \text{ J}$ | 1 kg |

780 Appendix C Impulse Depth- and Distance Dependency

781 Ford et al. (2014) found the following model to fit scaled blast impulse, distance
782 and depth:

$$\log_{10} \bar{I} = \beta_1 + \log_{10} \bar{r} + \beta_3 \bar{h} - \log_{10}(1 + 10^{10\beta_3 \bar{h}})/10 \quad (\text{C1})$$

783 Here \bar{h} is the scaled height of burst, and energy was specified in kg TNT. Changing to
784 scaled depth of explosion ($\bar{d} = -\bar{h}$), this can be written as

$$\bar{I}_1 = \frac{b_1}{\bar{r}} \frac{e^{-\bar{d}/\bar{d}_3}}{(1 + e^{-10\bar{d}/\bar{d}_3})^{1/10}} \quad (\text{C2})$$

785 Constants b_1 and \bar{d}_3 are listed in Table C1. Ford et al. present the scaled impulse mul-
786 tiplied by ambient reference pressure, which is different from this study where scaled im-
787 pulse is scaled overpressure integrated over energy-scaled time. We note that for $\bar{d} =$
788 $\bar{h} = 0$ the depth dependent part reduces to $2^{-0.1} \simeq 0.93$, which is about 7% different
789 from an exponential ($e^0 = 1$). For larger depths this difference is smaller, which justi-
790 fies the use of an exponential depth part (Appendix A) without the reducing factor which
791 is necessary above the surface:

$$\bar{I} = \frac{b_1}{\bar{r}} e^{-\bar{d}/\bar{d}_3} \quad (\text{C3})$$

792 Acknowledgments

793 The authors acknowledge NSF grant EAR-1420455 for funding the necessary blasting
 794 resources, and University at Buffalo for hosting a workshop during which experiments
 795 were conducted. Kayley Diem-Kay, Norman Yu and David Hyman are acknowledged for
 796 their assistance with experiment preparation and data recording.

797 The authors express appreciation to Kent Gee, Dept. of Physics and Astronomy
 798 at Brigham Young University (BYU) for providing the equipment used for the broad-
 799 band microphone measurements in this experiment. Funding for the BYU acoustical mea-
 800 surement team's participation came from the BYU College of Physical and Mathemat-
 801 ical Sciences that funded six undergraduate research assistant: Sarah Ostergaard, Eric
 802 Lynsenko, Grace McKay Smith, Christian Lopez, Carla Wallace, and Menley Hawkes;
 803 and the NSF-funded research Experience for Teachers hosted at BYU that allowed mid-
 804 dle school science teacher Julio Escobedo to play a pivotal role.

805 We thank Sean Maher and Richard Sanderson for their assistance with the seis-
 806 mic and infrasound field instrumentation preparation and deployment. Matoza acknowl-
 807 edges NSF grant EAR-1847736.

808 All measured data is hosted as datasets on VHub (vhub.org). A summarizing dataset
 809 which makes all data available is available at <https://vhub.org/resources/4710>. Data
 810 is also available separately as listed in the supporting information document (dataset S1).

811 References

- 812 Ahern, T. K., & Dost, B. (2012, August). *SEED Standard for the Exchange of*
 813 *Earthquake Data*. (Reference Manual No. Format version 2.4.). Retrieved from
 814 https://www.fdsn.org/pdf/SEEDManual_V2.4.pdf
- 815 Ambrosini, R. D., & Luccioni, B. M. (2006). Craters produced by explosions on
 816 the soil surface. *Journal of Applied Mechanics*, *73*(6), 890. doi: 10.1115/1
 817 .2173283
- 818 Ambrosini, R. D., Luccioni, B. M., Danesi, R. F., Riera, J. D., & Rocha, M. M.
 819 (2002, July). Size of craters produced by explosive charges on or above the
 820 ground surface. *Shock Waves*, *12*(1), 69–78. doi: 10.1007/s00193-002-0136-3
- 821 Antoun, T. H., Lomov, I. N., & Glenn, L. A. (2003, December). Simulation of the
 822 penetration of a sequence of bombs into granitic rock. *International Journal of*

- 823 *Impact Engineering*, 29(1-10), 81–94.
- 824 Arora, H., Del Linz, P., & Dear, J. (2017, June). Damage and deformation in com-
825 posite sandwich panels exposed to multiple and single explosive blasts. *Inter-*
826 *national Journal of Impact Engineering*, 104, 95–106. doi: 10.1016/j.ijimpeng
827 .2017.01.017
- 828 Boatwright, J. (1980). A spectral theory for circular seismic sources; simple esti-
829 mates of source dimension, dynamic stress drop, and radiated seismic energy.
830 *Bulletin of the Seismological Society of America*, 70(1), 1–27.
- 831 Bowman, D. C., Taddeucci, J., Kim, K., Anderson, J. F., Lees, J. M., Graettinger,
832 A. H., . . . Valentine, G. A. (2014). The acoustic signatures of ground accel-
833 eration, gas expansion, and spall fallback in experimental volcanic explosions.
834 *Geophysical Research Letters*, 41(6), 1916–1922. doi: 10.1002/2014GL059324
- 835 Bush, V., Conant, J. P., & Wilson, E. B. J. (1946). *Effects of Impact and Explosion*
836 (Technical Report No. AD0221586). Washington DC: Office of Scientific Re-
837 search and Development. Retrieved from [http://www.dtic.mil/get-tr-doc/
838 pdf?AD=AD0221586](http://www.dtic.mil/get-tr-doc/pdf?AD=AD0221586)
- 839 Büttner, R., & Zimanowski, B. (1998). Physics of thermohydraulic explosions. *Phys-*
840 *ical Review E*, 57(5), 5726–5729. doi: 10.1103/PhysRevE.57.5726
- 841 Crighton, D. G., & Scott, J. F. (1979, August). Asymptotic solutions of model equa-
842 tions in nonlinear acoustics. *Philosophical Transactions of the Royal Society of*
843 *London. Series A, Mathematical and Physical Sciences*, 292(1389), 101–134.
844 doi: 10.1098/rsta.1979.0046
- 845 Dillon, L. A. (1972). *The influence of soil and rock properties on the dimensions*
846 *of explosion-produced craters* (Technical Report No. AD0891964). New Mex-
847 ico: Air Force Weapons Laboratory, Air Force Systems Command Kirtland
848 Air Force Base. Retrieved from [http://www.dtic.mil/docs/citations/
849 AD0891964](http://www.dtic.mil/docs/citations/AD0891964)
- 850 Dürig, T., Gudmundsson, M., & Dellino, P. (2015). Reconstruction of the geometry
851 of volcanic vents by trajectory tracking of fast ejecta - the case of the Eyjaf-
852 jallajokull 2010 eruption (Iceland). *Earth, Planets and Space*, 67(1), 64. doi:
853 10.1186/s40623-015-0243-x
- 854 Dürig, T., Gudmundsson, M. T., Karmann, S., Zimanowski, B., Dellino, P., Rietze,
855 M., & Büttner, R. (2015). Mass eruption rates in pulsating eruptions esti-

- 856 mated from video analysis of the gas thrust-buoyancy transition—a case study
 857 of the 2010 eruption of Eyjafjallajökull, Iceland. *Earth, Planets and Space*,
 858 *67*(1), 1–17. doi: 10.1186/s40623-015-0351-7
- 859 Ehrgott, J., John Q., Akers, S. A., Windham, J. E., Rickman, D. D., & Danielson,
 860 K. T. (2011). The influence of soil parameters on the impulse and airblast
 861 overpressure loading above surface-laid and shallow-buried explosives. *Shock*
 862 *and Vibration*, *18*(6). doi: 10.3233/SAV-2010-0609
- 863 Fee, D., Waxler, R., Assink, J., Gitterman, Y., Given, J., Coyne, J., ... Grenard, P.
 864 (2013, June). Overview of the 2009 and 2011 Sayarim Infrasound Calibration
 865 Experiments: Sayarim Infrasound Overview. *Journal of Geophysical Research:*
 866 *Atmospheres*, *118*(12), 6122–6143. doi: 10.1002/jgrd.50398
- 867 Ford, S. R., Rodgers, A. J., Xu, H., Templeton, D. C., Harben, P., Foxall, W., &
 868 Reinke, R. E. (2014, March). Partitioning of seismoacoustic energy and
 869 estimation of yield and height-of-burst/depth-of-burial for near-surface explo-
 870 sions. *Bulletin of the Seismological Society of America*, *104*(2), 608–623. doi:
 871 10.1785/0120130130
- 872 Garces, M. (2018, October). Explosion source models. In *Infrasound monitoring for*
 873 *atmospheric studies* (pp. 273–345). Springer International Publishing. doi: 10
 874 .1007/978-3-319-75140-5_8
- 875 Garcés, M. A., Fee, D., & Matoza, R. S. (2013). *Modeling Volcanic Processes:*
 876 *The Physics and Mathematics of Volcanism* (S. A. Fagents, T. K. P. Gregg,
 877 & R. M. C. Lopes, Eds.). Cambridge: Cambridge University Press. doi:
 878 10.1017/CBO9781139021562
- 879 Gaudin, D., Taddeucci, J., Houghton, B. F., Orr, T. R., Andronico, D., Bello, E. D.,
 880 ... Scarlato, P. (2016, October). 3-D high-speed imaging of volcanic bomb tra-
 881 jectory in basaltic explosive eruptions. *Geochemistry, Geophysics, Geosystems*,
 882 *17*(10), 4268–4275. doi: 10.1002/2016gc006560
- 883 Gonnermann, H. M., & Manga, M. (2007). The fluid mechanics inside a volcano.
 884 *Annual Review of Fluid Mechanics*, *39*, 321–356. doi: 10.1146/annurev.fluid.39
 885 .050905.110207
- 886 Goto, A., Taniguchi, H., Yoshida, M., Ohba, T., & Oshima, H. (2001). Effects of
 887 explosion energy and depth to the formation of blast wave and crater: Field
 888 Explosion Experiment for the understanding of volcanic explosion. *Geophysical*

- 889 *Research Letters*, 28(22), 4287–4290. doi: 10.1029/2001GL013213
- 890 Grady, D. E. (1996). Shock-wave properties of brittle solids. In *AIP Conference Pro-*
 891 *ceedings* (Vol. 370, pp. 9–20). Seattle, Washington (USA): AIP. doi: 10.1063/
 892 1.50579
- 893 Graettinger, A. H., Valentine, G. A., & Sonder, I. (2015). Circum-crater variability
 894 of deposits from discrete, laterally and vertically migrating volcanic explosions:
 895 Experimental evidence and field implications. *Journal of Volcanology and*
 896 *Geothermal Research*, 308, 61–69. doi: 10.1016/j.jvolgeores.2015.10.019
- 897 Graettinger, A. H., Valentine, G. A., Sonder, I., Ross, P.-S., & White, J. D. L.
 898 (2015). Facies distribution of ejecta in analog tephra rings from experiments
 899 with single and multiple subsurface explosions. *Bulletin of Volcanology*, 77(8),
 900 1–12. doi: 10.1007/s00445-015-0951-x
- 901 Graettinger, A. H., Valentine, G. A., Sonder, I., Ross, P.-S., White, J. D. L., & Tad-
 902 deucci, J. (2014). Maar-diatreme geometry and deposits: Subsurface blast
 903 experiments with variable explosion depth. *Geochem. Geophys. Geosys.*, 15(3),
 904 740–764. doi: 10.1002/2013GC005198
- 905 Guzas, E. L., & Earls, C. J. (2010, August). Air blast load generation for simulating
 906 structural response. *Steel and Composite Structures*, 10(5), 429–455.
- 907 Holsapple, K. A., & Schmidt, R. M. (1980). On the scaling of crater dimensions:
 908 1. Explosive processes. *Journal of Geophysical Research*, 85(B12), 7247–7256.
 909 doi: 10.1029/JB085iB12p07247
- 910 Houghton, B. (2015). Explosive volcanism. In H. Sigurdsson, B. Houghton,
 911 S. R. McNutt, H. Rymer, & J. Stix (Eds.), *The encyclopedia of volcanoes*
 912 (Second ed., pp. 457–686). Elsevier LTD, Oxford.
- 913 Johnson, J., & Aster, R. (2005, December). Relative partitioning of acous-
 914 tic and seismic energy during Strombolian eruptions. *Journal of Vol-*
 915 *canology and Geothermal Research*, 148(3-4), 334–354. doi: 10.1016/
 916 j.jvolgeores.2005.05.002
- 917 Kim, K., & Rodgers, A. (2016, July). Waveform inversion of acoustic waves for ex-
 918 plosion yield estimation. *Geophysical Research Letters*, 43(13), 6883–6890. doi:
 919 10.1002/2016gl069624
- 920 Kim, K., & Rodgers, A. (2017, August). Influence of low-altitude meteorolog-
 921 ical conditions on local infrasound propagation investigated by 3-D full-

- 922 waveform modeling. *Geophysical Journal International*, 210(2), 1252–1263.
 923 doi: 10.1093/gji/ggx218
- 924 Kinney, G. F., & Graham, K. J. (1985). *Explosive shocks in air*. Springer.
- 925 Lee, C. K. B., & Mazzola, T. A. (1989). Ejecta scaling laws for craters in dry
 926 alluvial sites. *Journal of Geophysical Research: Solid Earth*, 94(B12), 17595–
 927 17605. doi: 10.1029/JB094iB12p17595
- 928 Lorenz, V. (1975). Formation of phreatomagmatic maar-diatreme volcanoes and its
 929 relevance to kimberlite diatremes. *Physics and Chemistry of the Earth*, 9(0),
 930 17–27. doi: 10.1016/0079-1946(75)90003-8
- 931 Macorps, É., Graettinger, A. H., Valentine, G. A., Ross, P.-S., White, J. D. L., &
 932 Sonder, I. (2016, March). The effects of the host-substrate properties on maar-
 933 diatreme volcanoes: Experimental evidence. *Bulletin of Volcanology*, 78(4).
 934 doi: 10.1007/s00445-016-1013-8
- 935 Maher, S. P., Matoza, R. S., Groot-Hedlin, C. D., Gee, K. L., Fee, D., & Yokoo,
 936 A. (2020, March). Investigating Spectral Distortion of Local Volcano Infra-
 937 sound by Nonlinear Propagation at Sakurajima Volcano, Japan. *Journal of*
 938 *Geophysical Research: Solid Earth*, 125(3). doi: 10.1029/2019JB018284
- 939 Mammadova, N., Ghaisas, S., Zenitsky, G., Sakaguchi, D. S., Kanthasamy, A. G.,
 940 Greenlee, J. J., & West Greenlee, M. H. (2017, July). Lasting Retinal Injury in
 941 a Mouse Model of Blast-Induced Trauma. *The American Journal of Pathology*,
 942 187(7), 1459–1472. doi: 10.1016/j.ajpath.2017.03.005
- 943 Marchetti, E., Ripepe, M., Delle Donne, D., Genco, R., Finizola, A., & Garaebiti,
 944 E. (2013, November). Blast waves from violent explosive activity at Yasur
 945 Volcano, Vanuatu. *Geophysical Research Letters*, 40(22), 5838–5843. doi:
 946 10.1002/2013GL057900
- 947 Matoza, R. S., Arciniega-Ceballos, A., Sanderson, R. W., Mendo-Pérez, G., Rosado-
 948 Fuentes, A., & Chouet, B. A. (2019, January). High-broadband seismoacoustic
 949 signature of vulcanian explosions at Popocatépetl volcano, Mexico. *Geophysical*
 950 *Research Letters*, 46(1), 148–157. doi: 10.1029/2018gl080802
- 951 Matoza, R. S., Fee, D., & Lopez, T. M. (2014, November). Acoustic Charac-
 952 terization of Explosion Complexity at Sakurajima, Karymsky, and Tungu-
 953 rahua Volcanoes. *Seismological Research Letters*, 85(6), 1187–1199. doi:
 954 10.1785/0220140110

- 955 Matoza, R. S., Garcés, M. A., Chouet, B. A., D’Auria, L., Hedlin, M. A. H.,
 956 De Groot-Hedlin, C., & Waite, G. P. (2009, April). The source of infrasound
 957 associated with long-period events at Mount St. Helens. *Journal of Geophysical*
 958 *Research*, *114*(B4), B04305. doi: 10.1029/2008JB006128
- 959 Muhlestein, M. B., Gee, K. L., & Macedone, J. H. (2012, March). Educational
 960 demonstration of a spherically propagating acoustic shock. *The Journal of the*
 961 *Acoustical Society of America*, *131*(3), 2422–2430. doi: 10.1121/1.3676730
- 962 Park, I., Jolly, A., Matoza, R. S., Kennedy, B., Kilgour, G., Johnson, R., . . . Ce-
 963 vuard, S. (2021, September). Seismo-acoustic characterisation of the 2018
 964 Ambae (Manaro Voui) eruption, Vanuatu. *Bulletin of Volcanology*, *83*(9), 60.
 965 doi: 10.1007/s00445-021-01474-z
- 966 Pistolesi, M., Delle Donne, D., Pioli, L., Rosi, M., & Ripepe, M. (2011). The 15
 967 March 2007 explosive crisis at Stromboli volcano, Italy: Assessing physical
 968 parameters through a multidisciplinary approach. *Journal of Geophysical*
 969 *Research: Solid Earth*, *116*(B12). doi: 10.1029/2011JB008527
- 970 Qiu, X., Shi, X., Gou, Y., Zhou, J., Chen, H., & Huo, X. (2018, April). Short-delay
 971 blasting with single free surface: Results of experimental tests. *Tunnelling and*
 972 *Underground Space Technology*, *74*, 119–130. doi: 10.1016/j.tust.2018.01.014
- 973 Rogers, P. H. (1977). Weak-shock solution for underwater explosive shock waves.
 974 *The Journal of the Acoustical Society of America*, *62*(6), 1412. doi: 10.1121/1
 975 .381674
- 976 Ross, P.-S., White, J. D. L., Valentine, G. A., Taddeucci, J., Sonder, I., &
 977 Andrews, R. G. (2013). Experimental birth of a maar-diatreme vol-
 978 cano. *Journal of Volcanology and Geothermal Research*, *260*, 1–12. doi:
 979 10.1016/j.jvolgeores.2013.05.005
- 980 Sato, H., & Taniguchi, H. (1997). Relationship between crater size and ejecta vol-
 981 ume of recent magmatic and phreato-magmatic eruptions: Implications for
 982 energy partitioning - range. *Geophysical Research Letters*, *24*(3), 205–208. doi:
 983 10.1029/96GL04004
- 984 Schnurr, J., Kim, K., Garces, M. A., & Rodgers, A. (2020, May). Improved Para-
 985 metric Models for Explosion Pressure Signals Derived From Large Datasets.
 986 *Seismological Research Letters*, *91*(3), 1752–1762. doi: 10.1785/0220190278
- 987 Sonder, I., Graettinger, A. H., & Valentine, G. A. (2015). Scaling multiblast craters:

- 988 General approach and application to volcanic craters. *Journal of Geophysical*
989 *Research, Solid Earth*, 120(9), 6141–6158. doi: 10.1002/2015JB012018
- 990 Strange, J. N., Denzel, C. W., & McLane, T. I., III. (1960). *Cratering from high*
991 *explosive charges. Analysis of crater data* (Tech. Rep. No. AD0263170).
992 Vicksburg, MS: Army Engineer Waterways Experiment Station. Retrieved
993 from [http://oai.dtic.mil/oai/oai?verb=getRecord&metadataPrefix=](http://oai.dtic.mil/oai/oai?verb=getRecord&metadataPrefix=html&identifier=AD0263170)
994 [html&identifier=AD0263170](http://oai.dtic.mil/oai/oai?verb=getRecord&metadataPrefix=html&identifier=AD0263170)
- 995 Taddeucci, J., Peña Fernández, J. J., Cigala, V., Kueppers, U., Scarlato, P.,
996 Del Bello, E., ... Panunzi, S. (2021, August). Volcanic Vortex Rings:
997 Axial Dynamics, Acoustic Features, and Their Link to Vent Diameter
998 and Supersonic Jet Flow. *Geophysical Research Letters*, 48(15). doi:
999 10.1029/2021GL092899
- 1000 Taddeucci, J., Sottili, G., Palladino, D., Ventura, G., & Scarlato, P. (2010). A note
1001 on maar eruption energetics: Current models and their application. *Bulletin of*
1002 *Volcanology*, 72(1), 75–83. doi: 10.1007/s00445-009-0298-2
- 1003 Taylor, Z. J., Gurka, R., Kopp, G. A., & Liberzon, A. (2010). Long-duration time-
1004 resolved PIV to study unsteady aerodynamics. *IEEE JIM*, 59(12), 3262–3269.
1005 doi: 10.1109/TIM.2010.2047149
- 1006 Valentine, G. A., Graettinger, A. H., Macorps, É., Ross, P.-S., White, J. D. L.,
1007 Döhring, É., & Sonder, I. (2015). Experiments with vertically and lat-
1008 erally migrating subsurface explosions with applications to the geology of
1009 phreatomagmatic and hydrothermal explosion craters and diatremes. *Bulletin*
1010 *of Volcanology*, 77(3). doi: 10.1007/s00445-015-0901-7
- 1011 Valentine, G. A., Graettinger, A. H., & Sonder, I. (2014). Explosion depths for
1012 phreatomagmatic eruptions. *Geophysical Research Letters*, 41(9), 3045–3051.
1013 doi: 10.1002/2014GL060096
- 1014 Valentine, G. A., White, J. D. L., Ross, P.-S., Amin, J., Taddeucci, J., Sonder, I.,
1015 & Johnson, P. J. (2012). Experimental craters formed by single and multiple
1016 buried explosions and implications for maar-diatreme volcanoes. *Geophysical*
1017 *Research Letters*, 39, L20301. doi: 10.1029/2012GL053716
- 1018 Voight, B. (1981). Time scale for the first moments of the May 18 eruption. In
1019 P. W. Lipman & D. R. Mullineaux (Eds.), *The 1980 eruptions of mount st.*
1020 *Helens, washington* (Vol. 1250, pp. 69–93). U.S. Government Printing Office.

- 1021 Vortman, L. J. (1968). Craters from surface explosions and scaling laws. *Journal of*
1022 *Geophysical Research*, 73(14), 4621–4636. doi: 10.1029/JB073i014p04621
- 1023 Young, S. M., Gee, K. L., Neilsen, T. B., & Leete, K. M. (2015, September). Out-
1024 door measurements of spherical acoustic shock decay. *The Journal of the*
1025 *Acoustical Society of America*, 138(3), EL305-EL310. doi: 10.1121/1.4929928
- 1026 Zhou, J., Lu, W., Yan, P., Chen, M., & Wang, G. (2016, October). Frequency-
1027 Dependent Attenuation of Blasting Vibration Waves. *Rock Mechanics and*
1028 *Rock Engineering*, 49(10), 4061–4072. doi: 10.1007/s00603-016-1046-5